Influence of material extrusion parameters on fracture mechanisms of polylactic acid under three-point bending

Mario Álvarez-Blanco [a], Adrián Arias-Blanco [a], Diego Infante-García [b,*],
Miguel Marco [a], Eugenio Giner [b], M. Henar Miguélez [a]

[a] Department of Mechanical Engineering, Universidad Carlos III de Madrid, Avda. de la Universidad 30, 28911 Leganés, Madrid, Spain
[b] Institute of Mechanical and Biomechanical Engineering – I2MB, Department of Mechanical Engineering and Materials, Universitat Politècnica de València. Camino de Vera, 46022 Valencia, Spain

ABSTRACT

In this work, a thorough fracture assessment of additive manufactured specimens made by 3D printed polylactic acid (PLA) under three-point bending is presented. This polymer is widely used in additive manufacturing for numerous applications, gaining prominence in fields such as biomechanics. Prismatic fully dense specimens and lattice structure specimens with different raster orientations and densities were fabricated using the material extrusion-based additive manufacturing technique. The objective is to analyse the effect of relevant process parameters on the fracture mechanism of short beam specimens tested under three-point bending. Digital image correlation and computed tomography have been used to measure the full field displacement and internal defects, respectively. Furthermore, the theory of critical distances was applied to assess the mechanical strength of lattice structure specimens. The results have shown the strong influence of raster orientation on the mechanical strength and fracture patterns even for negative air gap values. The transition from brittle to ductile failure was observed when changing density and raster orientation. Lastly, neck-shaped defects were detected in knots of specimens manufactured with a grid pattern. Defects in grid pattern specimens appear due to the prescribed path followed by the extruder during the building process. They were the main source causing a decrease in the mechanical strength and fracture trajectories. The objective of this research is to enhance the knowledge on the mechanical response of 3D printed components and to give an in-depth failure assessment.

1. Introduction

Additive manufacturing (AM) is the process of bonding materials to create objects from digital 3D models, usually layer-by-layer, according to ISO/ASTM 52900:2021. During the last decades, AM has increased efficiency for rapid prototyping of components with complex geometries. Furthermore, material waste minimization, lightweight production capability and part customization are some of the main features that makes AM a potential fabrication technology in aerospace industry and medical applications [1,2].

According to the standard ISO/ASTM 52900:2021, material extrusion (MEX) is an AM process in which feedstock is selectively dispensed through a nozzle. A common MEX process, also known as fused filament fabrication or fused deposition modelling, involves

Nomenclature

|	
3P	three-point
a	sample length
AM	additive manufacturing
b	sample width
DIC	digital image correlation
E^{3P}	flexural elastic modulus
E_{tan}	instantaneous tangent elastic modulus
E^{UT}	tensile elastic modulus
FEA	finite element analysis
F_{max}	maximum force
G	shear modulus
GP	grid pattern
h	sample height
K	flexural stiffness
K_c	fracture toughness
L	bending supports distance
L_c	critical distance
MEX	material extrusion
PLA	polylactic acid
s	deflection at central loading
s_{fl}	flexural deflection
s_{sh}	shear deflection
TCD	theory of critical distances
UT	uniaxial tensile
ϵ	nominal strain
ν	Poisson's ratio
σ_{max}^{3P}	flexural strength
σ_o	inherent or critical stress
σ_y	tensile strength at yield
τ_{max}^{3P}	maximum shear stress
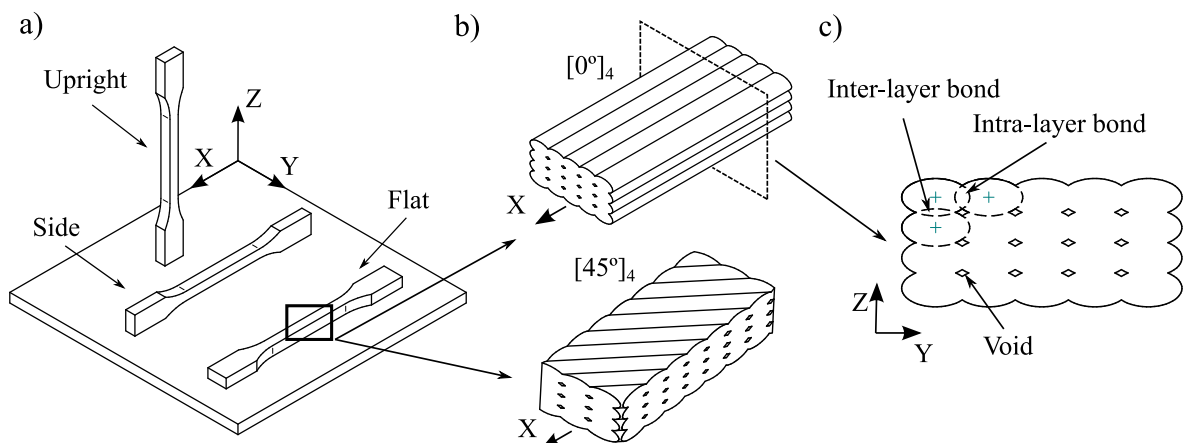
Fig. 1. a) Schematic representation of different building directions in tensile specimens, b) mesostructure representation showing different raster orientations (0° and 45°) of 4 layers and c) idealised cross-section view of $[0°]_4$ (plane YZ).

feeding a filament, commonly a thermoplastic, into an extruder head where the material is heated and forced out through an orifice onto a build platform. The viscous material is deposited following a predefined path, which is commonly fan-cooled or air-cooled depending on the feedstock, creating a thin cross-sectional track which bonds to adjacent lines and previous layer [3].

During the last decades, significant research has been carried out on the MEX process optimization to improve the mechanical properties of components [3–11], thus, promoting the implementation of MEX process in the manufacturing of end products, instead of

prototypes, able to withstand service loads [9]. The mechanical behaviour can be studied under quasi-static conditions (e.g. using tensile tests [12–19], compression [20,21], shear [22] or flexural tests [18,21,23–26], focusing typically on measurement of the elastic modulus, material strength, fracture toughness or hardness [27,28]. On the other hand, under cyclic loading or dynamic conditions, fatigue and creep tests are used to assess S-N diagrams of alternating stress versus number of cycles to failure or material relaxation times, respectively [5,9,29].

A large number of parameters affects the MEX process of part quality in terms of mechanical properties, making the process optimization not trivial. The most relevant parameters are slicing parameters (e.g., layer thickness, raster orientation, flow rate, etc.), building orientation and temperature conditions [5]. Note that these parameters are significantly dependent on MEX feedstock. In this way, the process optimization must be performed after any alteration of the feedstock. Moreover, pressure and temperature fluctuations at nozzle are likely to happen during MEX process due to insufficient *in-situ* monitoring control in most 3D printers [30], which may lead to inconsistent extrusion.

In general, most of the previous works found in the literature have reported a significant anisotropy of mechanical properties in MEX specimens [9,18,31,32]. The building orientation and raster orientation with respect to the loading direction (see Fig. 1a) are the main parameters affecting the mechanical anisotropy in MEX samples. In general, tensile specimens tested along the building direction (upright specimen in Fig. 1a) show a lower tensile strength than specimens built in the side or flat orientation. On the other hand, specimens tested in the raster deposition direction (0°) commonly present a larger tensile strength than other raster orientation configurations. These outcomes have suggested that normal directions to planes produced due to the bonding between adjacent deposited lines or strands, both inter-layer and intra-layer bonds, are weaker than the direction of strands. Additionally, fracture patterns found in MEX parts usually tend to follow preferentially these bonding planes [31,33]. In addition, defects such as voids (see Fig. 1c) can be found in MEX parts [34], acting as stress raisers and directly decreasing the effective strength of specimens. The main effect of internal voids can be the intensification of the mechanical anisotropy as well as the decrease of the mechanical strength of MEX parts. One of the relevant parameters affecting porosity and intra-layer bond strength is the air gap. Negative values of air gap between adjacent strands reduce the void formation, although it increases the building time [31,35–37].

In terms of fracture characterization, Lampron et al. [18] tested unidirectional PLA single edge notched bending specimens (SENB). The specimens showed a ductile fracture for cross-layer crack propagation and brittle behaviour for inter-layer fracture. Allum et al. [17] reported that the main factor affecting the mechanical anisotropy was the filament-scale geometric features caused by the printing process itself rather than the weak-inter-filament bonding. However, the review presented by Gao et al. [32] pointed out that the interlayer bond quality is a function of the bond time due to the deposition of the feedstock. This bond time dominates the inter-diffusion and entanglements between two adjacent strands. Ayatollahi et al. [38] experimentally characterised the fracture behaviour of semi-circular bending PLA specimens manufactured with four different raster angles (0°/90°, 15°/-75°, 30°/-60° and 45°/-45°). They concluded that the best performance was obtained for the 45°/-45° specimen. Marsavina et al. [39] appreciated that the crack propagation process in SENB specimens took place as a stepwise process in which the use of larger fibres can improve the strength of the component. Other experimental studies are focused on the effect of different printing parameters such as the thickness layer [40] or the printing interlayer waiting time [41]. On the other hand, in terms of static strength and fracture toughness prediction, the theory of critical distances (TCD) [14,15,42,43] and the averaged strain energy density (ASED) [42] are among the methods which have successfully estimated the load bearing capacity of PLA MEX components. For a more detailed review of the topic, we refer the reader to [9,44,45].

Several research gaps are found after reviewing the literature, such as the difficulty to establish proper comparisons between experimental mechanics works due to the lack of standard test methods and the large variety of feedstock materials and 3D printer manufacturers. Additionally, there are some controversial results regarding the main cause affecting the mechanical anisotropy of the tests [9,17,44–47]. Lastly, the experiments are usually performed using dog-bone specimens under uniaxial tension or analysing fully dense specimens (i.e., infill is usually not considered). In this way, it is necessary a meaningful explanation of the static mechanical and fracture behaviour of MEX parts under more realistic loading conditions in order to perform an efficient mechanical optimization.

This work focuses on the fracture assessment of MEX prismatic specimens made of PLA tested under three-point bending, analysing both fully dense bulk and lattice structure specimens. Experimental testing together with numerical modelling are both used in order to analyse the failure mechanism in 3D printed specimens with different raster manufacturing configurations. A more detailed assessment of printing defects using non-destructive techniques such as 3D computed tomography along with full field displacement measurement using digital image correlation is performed in order to study essential features that affect the failure mechanisms.

2. Materials and methods

This section describes the design and manufacturing of the specimens and the numerical and experimental methodology used in this work. PLA prismatic specimens were manufactured using different process parameters and tested under three-point (3P) bending. Additionally, dog-bone shaped specimens were manufactured and tested under uniaxial tensile (UT) loading. A finite element analysis (FEA) was carried out to assess the local stress fields and to apply the theory of critical distances (TCD).

2.1. Design and manufacturing of specimens

PLA filament (CAS RN 9051-89-2) with a mean diameter of 2.85 mm and a density of 1.24 g/cm^3 was supplied by BCN3D (BCN3D Technologies Inc., Barcelona, Spain). All material extruded parts were manufactured by the MEX-type 3D printer BCN3D Epsilon W50. A 1 mm diameter nozzle was used in the process. The specimens were made with a layer thickness of 0.4 mm, without top and bottom

Table 1

Process parameters.

Parameter	Value
Nozzle diameter [mm]	1.0
Layer thickness [mm]	0.4
Line width [mm]	1.0
Air gap [mm]	−0.1
Print speed [mm/s]	40.0
Printing temperature [°C]	200
Build platform temperature [°C]	40

Table 2

Test code, description of specimens and mean weight (variation coefficient of mean weight was below 5% for all tests).

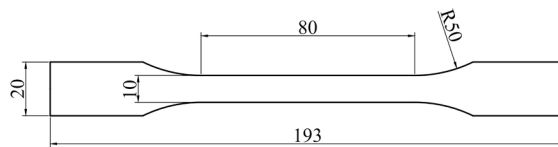| Test code	Type of test	Infill density [%]	Raster orientation	Mean weight [g]
UT_D100_00	UT	100	$[0°]_{10}$	14.30
3P_D100_00	3P	100	$[0°]_{20}$	20.83
3P_D100_90	3P	100	$[90°]_{20}$	20.78
3P_D100_45	3P	100	$[45°]_{20}$	20.80
3P_D100_45X	3P	100	$[45°/-45°]_{10}$	20.88
3P_D87_GP	3P	87	GP	16.60
3P_D58_GP	3P	58	GP	11.38
3P_D29_GP	3P	29	GP	5.98

Fig. 2. Dimensional drawing of UT_D100_00 specimen (4 mm thickness).

layers and walls to create homogeneous sheets along the whole geometry. All other process parameters were set as default following the material supplier's recommendations.

Table 1 lists some important features used for the manufacturing of the test samples. Two different specimens were manufactured: dog-bone and prismatic specimens tested for UT and 3P bending, respectively. In the case of prismatic samples, fully dense specimens with four different raster orientations and lattice structure specimens with three different densities using a grid pattern (GP) were manufactured. Table 2 exhibits all the specimens tested in this work and the process parameters analysed (raster orientation and infill density). Raster orientation refers to the angle between the raster deposition direction and the specimen longitudinal direction (see Fig. 1b). The subscript indicates the number of extruded layers of the sample. In the case of the prismatic specimens for 3P bending tests with 100% density, the similarity of their weights ensures a precise printing design (same amount of deposited filament).

2.1.1. Dog-bone specimen for tensile testing

The dog-bone shaped specimen (UT_D100_00) with 100% density (fully dense) and raster orientation at 0° is tested under UT loading for the characterization of the extruded material. ISO 527 standards [48,49] establish the conditions for the testing of polymers and provides standard designs for tensile samples. However, these specifications are defined for traditional manufacturing of thermoplastics such as injection moulding. As Özen et al. [50] reported in their investigation, the manufacturing of dog-bone specimens via MEX is not a simple task and some adjustments from standards must be considered.

The suggested dimensions in standards usually cause invalid results in 3D printed parts when using default process parameters. Due to the infill pattern and printing defects (e.g. discretization of radius) the stress concentration produced by the cross-section change may lead to premature specimen failure [31]. Therefore, the radius was increased up to 50 mm to relieve stress concentration (see Fig. 2 for specimen geometry), while keeping the rest of the initial dimensions at the middle region and a total thickness of 4 mm according to ISO 527 [48,49]. Thus, a theoretical stress concentration factor of 1.053 was obtained via a 2D FEA under plane strain conditions. In total, 4 dog-bone specimens were tested to ensure the repeatability of the experimental results.

2.1.2. Prismatic specimens tested under three-point bending

For the 3P bending test, 28 prismatic specimens were manufactured with seven different designs (four specimens per condition). Process parameters are listed in Table 2. The specimen geometry is a rectangular prism with a length a of 100 mm, a height h of 20 mm and a width b of 8 mm (depicted in Fig. 3a). This particular width value was chosen to obtain exactly 20 layers of 0.4 mm thickness. These samples were made without wall lines or top and bottom layers, i.e. no material is deposited along the perimeter.
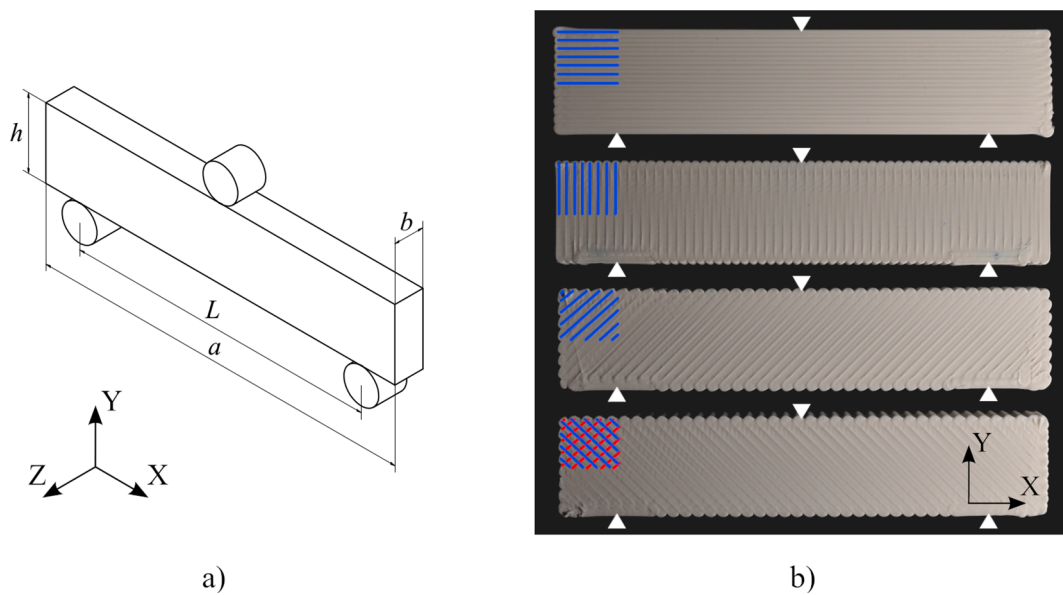
Fig. 3. a) Arrangement of prismatic specimen in 3P bending test and dimensional parameters. b) Fully dense prismatic specimens with the corresponding raster orientations sketched and location of loading pins in 3P bending test (from top to bottom: 3P_D100_00, 3P_D100_90, 3P_D100_45 and 3P_D100_45X).
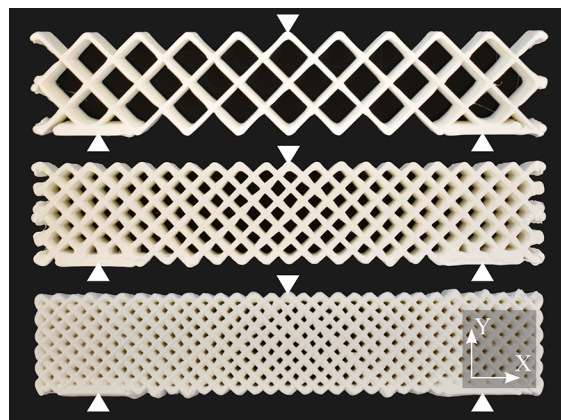

Fig. 4. GP prismatic specimens and location of loading pins in 3P bending test (from top to bottom: 3P_D29_GP, 3P_D58_GP and 3P_D87_GP).

Firstly, four models with 100% infill density prismatic samples (fully dense specimens) were manufactured in flat position. The difference between each specimen is the angle of the raster with respect the horizontal direction of the flexural test (raster orientation). As outlined in Table 2, the raster orientations analysed are: $[0°]_{20}$ (3P_D100_00), $[90°]_{20}$ (3P_D100_90), $[45°]_{20}$ (3P_D100_45) and $[-45°/45°]_{10}$ (3P_D100_45X). Fig. 3b shows these 3D printed specimens with the specific raster orientations plotted on them.

Next, three models with lattice structure were designed using a GP profile. The GP is usually one of the most common choices for lightening MEX parts. In this work, we decided to remove the walls, bottom and top layers to evaluate the mechanical behaviour and failure of the infill core itself. Following the dimensions of the rectangular prism (100 mm × 20 mm × 8 mm), the core was filled with a squared GP. The grid lines were printed with a single 1 mm thick strand. The measures of this lattice define the infill density of the samples. As shown in Table 2, the density percentages of these specimens are 29% (3P_D29_GP), 58% (3P_D58_GP) and 87% (3P_D87_GP). Densities were chosen in such a way that the number of cells was a whole number for each specimen in the height direction. The three GP specimens are shown in Fig. 4.

Note that the contact point with the upper pin of the bending tool must be coincident with a corner of the lattice structure to maintain the requested cross-section. In addition, benefiting from the inherent freedom in the AM design, two flat supports at the bottom sides were necessary to ensure a proper load transmission between the specimen and the lower pins of the bending tool.
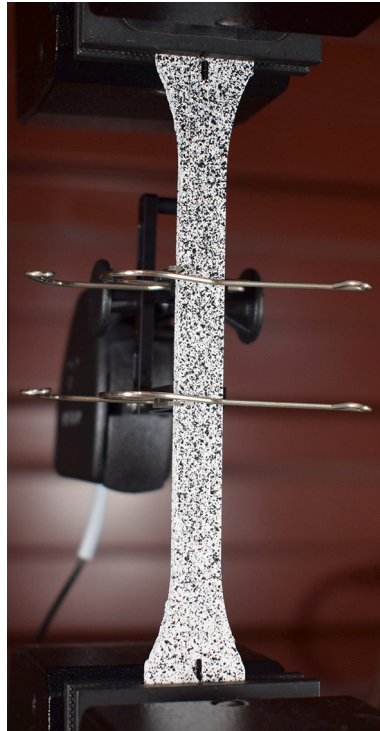
Fig. 5. Experimental setup of the UT test for UT_D100_00 specimen with speckled pattern and clip-on extensometer.

2.2. Experimental tests

The mechanical testing of the aforementioned specimens was performed in the laboratory to characterise the extruded material. The experimental setup is explained in this subsection.

2.2.1. Mechanical testing procedures

The experimental tests were carried out in the electromechanical testing machine Instron 3366, using 500 N and 10 kN load cells. All specimens were kept under the same conditions and time until testing. Four samples were manufactured for each of the eight specimen types of Table 2 to ensure the repeatability of the results. The nomenclature adopted for these replications was *Nx*, where × is the number of the replicated sample (up to 4). In total, 32 specimens were fabricated and tested in this work.

2.2.1.1. Uniaxial tensile test. Regarding the UT test, ISO 527 standards for thermoplastic materials [48,49] was used as a reference. The static axial clip-on extensometer Instron 2630-107 was employed to obtain the strain along the longitudinal direction of the dog-bone specimen. Test velocity was set to 1 mm/min to ensure quasi-static conditions. Fig. 5 shows the test setup with a speckled dog-bone specimen to apply digital image correlation (DIC).

2.2.1.2. Three-point bending test. In the case of the 3P bending test, prismatic specimens were tested until complete failure following ISO 178 standard [51] as a reference. The crosshead velocity was set to 0.53 mm/min, thus, the strain rate did not exceed 1% min^{-1} ensuring quasi-static conditions for all designs. A bending rig with a distance between supports *L* of 80 mm and three pins of 10 mm diameter were employed for these tests. As mentioned, upper pin of the tool matched the upper midplane corner of the lattice structure in the GP specimens. The experimental setup with the instrumentation involved in the laboratory is shown in Fig. 6 (top).

2.2.2. Digital image correlation

The measurement of the full displacement and strain fields on the surface of the samples was carried out through DIC. This technique was implemented using MultiDIC software [52] and two high resolution digital cameras (Nikon D3300, 24 megapixels). The setup during the 3P bending test and images taken by each camera are shown in Fig. 6 (bottom).

2.3. Static strength assessment via the theory of critical distances and finite element modelling of 3P bending tests

For the 3P bending test arrangement shown in Fig. 6, the stress state in the horizontal direction at the middle section changes linearly from tension at the bottom side to compression at the top side. Additionally, the shear stress shows a parabolic distribution

Fig. 6. Experimental setup of the 3P bending test for prismatic specimens with DIC instrumentation (top) and captures from each camera (bottom).

along the cross-section of the beam (see Eqs. (1) and (2) for maximum values of extensional stress or flexural strength σ_{max}^{3P} and shear stress τ_{max}^{3P} in 3P bending tests at the middle section), e.g. [53]. These expressions are a function of the maximum force F_{max}, the distance between supports L and the cross-section dimensions b and h.

$$\sigma_{max}^{3P} = \frac{3}{2} \frac{F_{max} L}{bh^2} \tag{1}$$

$$\tau_{max}^{3P} = \frac{3}{4} \frac{F_{max}}{bh} \tag{2}$$

Short-beam specimens may fail due to compression on the top face, shear stresses at the middle section or tensile stress at the bottom face. In this work, according to specimen dimensions, σ_{max}^{3P} is eight times τ_{max}^{3P}. The beam deflection, at the central loading, s can be considered as the addition of two components: flexural deflection s_{fl} and shear deflection s_{sh}.

$$s_{fl} = \frac{1}{4} \frac{FL^3}{Ebh^3} \tag{3}$$

$$s_{sh} = \frac{0.3FL}{Gbh} \tag{4}$$

Where $G = E/(2(1 + \nu))$ represents the shear modulus, E the elastic modulus and ν the Poisson's ratio. Considering a homogeneous, linear isotropic material, it is possible to estimate the apparent elastic modulus under 3P bending by means of s_{fl} and s_{sh} as follows.

$$E^{3P} = \left(\frac{1}{4} \frac{L^3}{bh^3} + 0.6 \frac{(1 + \nu)L}{bh} \right) K \tag{5}$$

being K the experimentally measured flexural stiffness of each specimen (defined by the ratio between experimental measures of force and deflection in quasi-linear regime). Note that this theory neglects the effect of contact stresses due to loading pins. In this way, the stress state is supposed to be complex near these regions [53]. In addition, the application of previous equations for GP specimens is
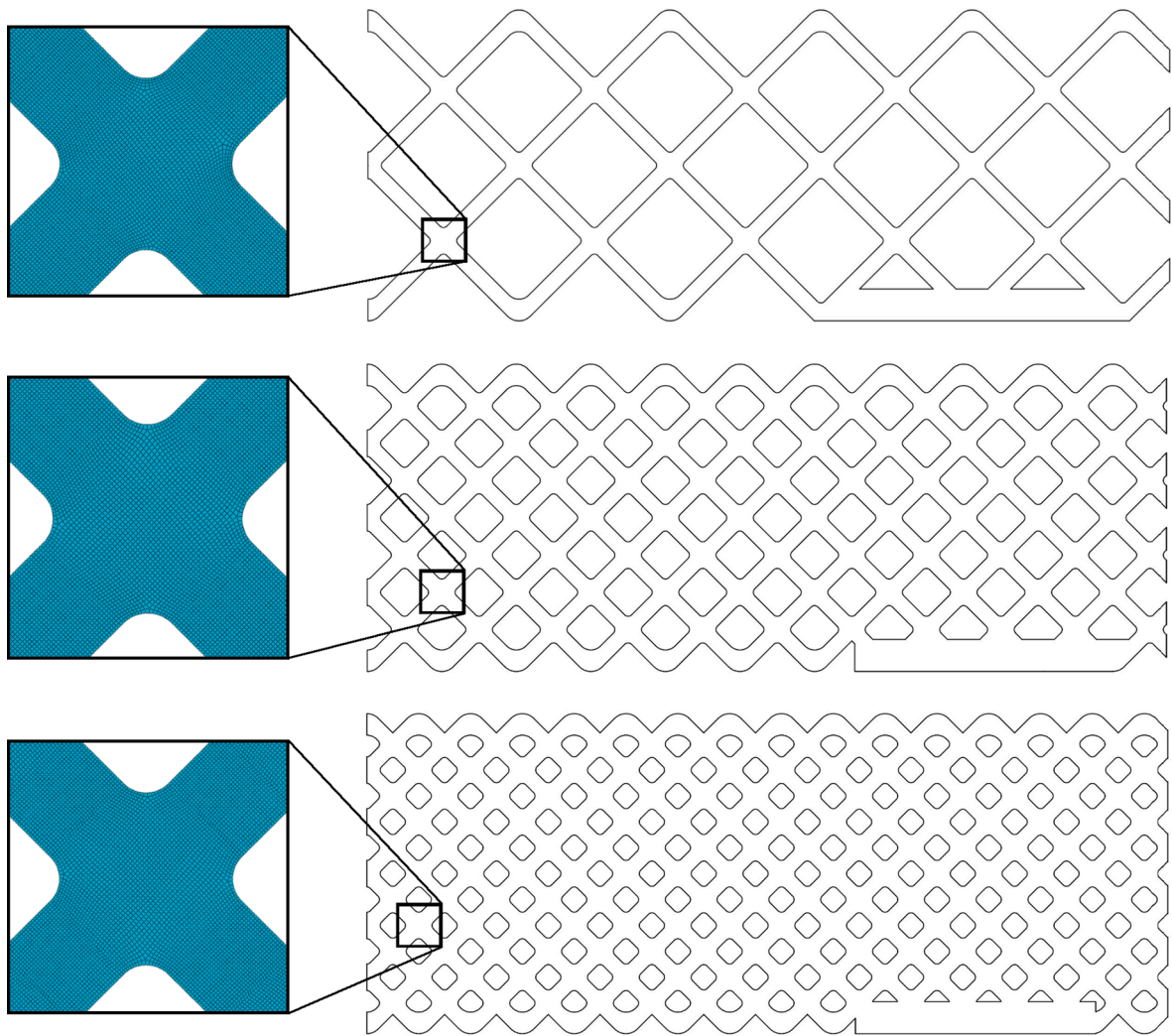
Fig. 7. Numerical models and detail of their mesh. From top to bottom: 3P_D29_GP, 3P_D58_GP and 3P_D87_GP.

Table 3
Mesh parameters of numerical models.

Model	Approx. elem. size [mm]	Number of elements
D29	0.03	164,340
D58	0.03	284,686
D87	0.03	358,176

not appropriate because it does not incorporate the lattice structure of the sample. However, it can be useful to give a preliminary insight into the mechanical properties, such as in a homogenization process.

In order to assess the full stress and strain fields and to apply the TCD, FEA of the most relevant 3P bending tests were carried out in Abaqus Standard. Three numerical models were created for the corresponding GP specimens (3P_D29_GP, 3P_D58_GP and 3P_D87_GP) with full details of the mesostructure.

The mechanical properties of the tested material obtained experimentally in the uniaxial test were used. PLA was considered as a linear elastic isotropic material, following the assumption of small-scale yielding [14,15,42,43]. The specimen geometry and loading allow symmetry conditions in the middle of the flexural test. In addition, a 2D plane strain condition was considered. Fig. 7 shows the GP specimen designs used for the FEA-based simulations and mesh details.

The mesh was refined in the middle region between the supports, leaving the remaining area with an approximate element size of 0.25 mm. The element size in the refined zone was chosen seeking the optimal compromise between accuracy of results and computational cost. For this purpose, a mesh sensitivity analysis was carried out comparing four consecutive sizes from 0.015 to 0.050
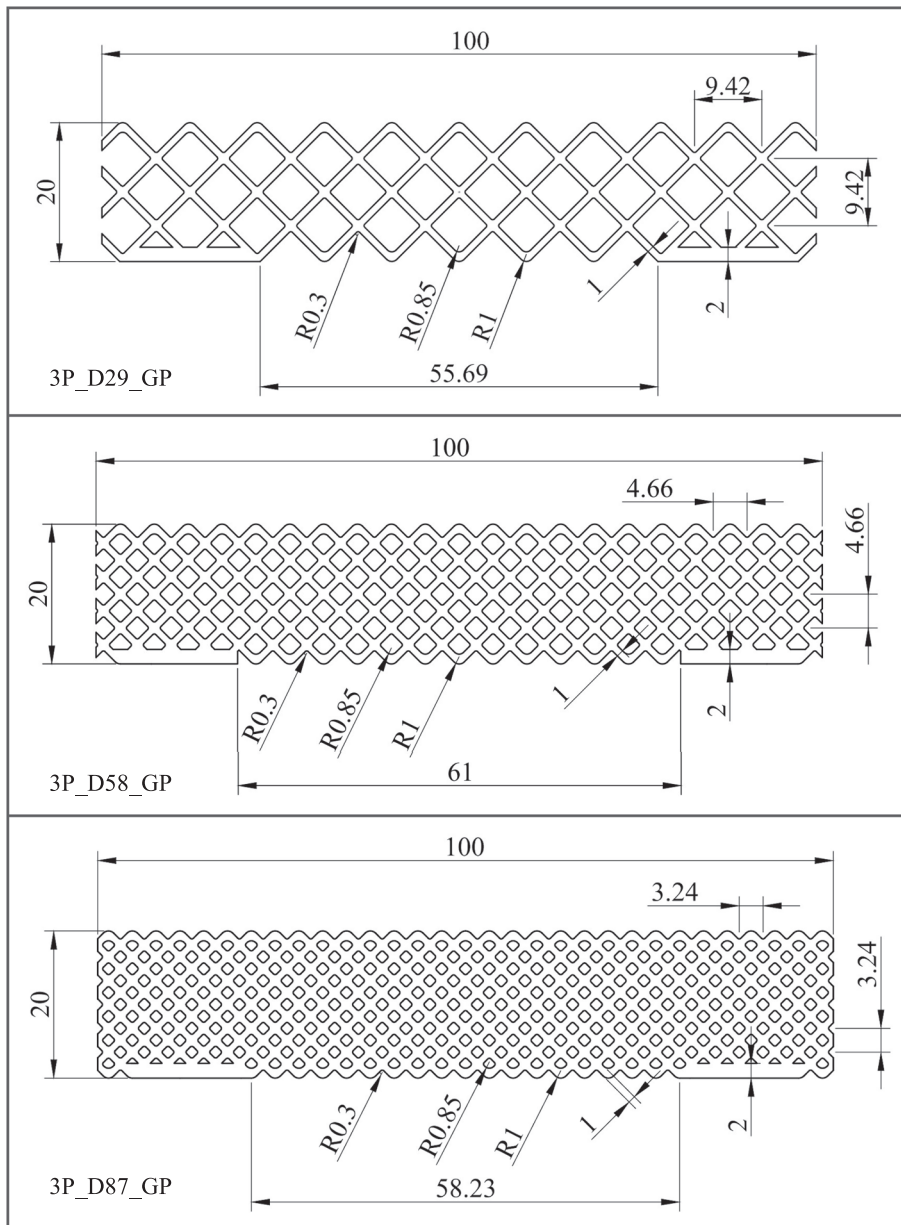
Fig. 8. Dimensional drawings of GP specimens (8 mm thickness).

mm. The maximum admissible error was 2.5% of the maximum principal stress at the point of application of TCD ($L_c/2$ from the hot-spot and perpendicular to the free surface). Quadrilateral elements (code CPE4R in Abaqus) were used. Some mesh parameters are compiled in Table 3. Note that the approximate element size for the GP specimens was considerably reduced due to the lattice and fillet radius dimensions. This value was fixed for the three models to ensure a reliable comparison of their numerical results.

Assuming the cross-joints of the GP specimens behave as notches of finite radius in the prismatic geometry (see Fig. 8), TCD was implemented during post-processing. In particular, the point method is used to apply the hypothesis in simple terms. Stated by Taylor [54], among others, this estimation postulates that the failure of a part including a stress raiser (notched sample, in this case) will occur when a specific stress value at a certain distance $L_c/2$ from the notch tip is reached. Once this inherent or critical stress σ_o is calculated, the critical area analysed in the model will be located on the perpendicular ($L_c/2$ length) from the node in the notch root where the maximum stress is focused. The dimension L_c is the so-called critical distance, being a function of the aforementioned critical stress σ_o and the fracture toughness K_c of the material as follows:

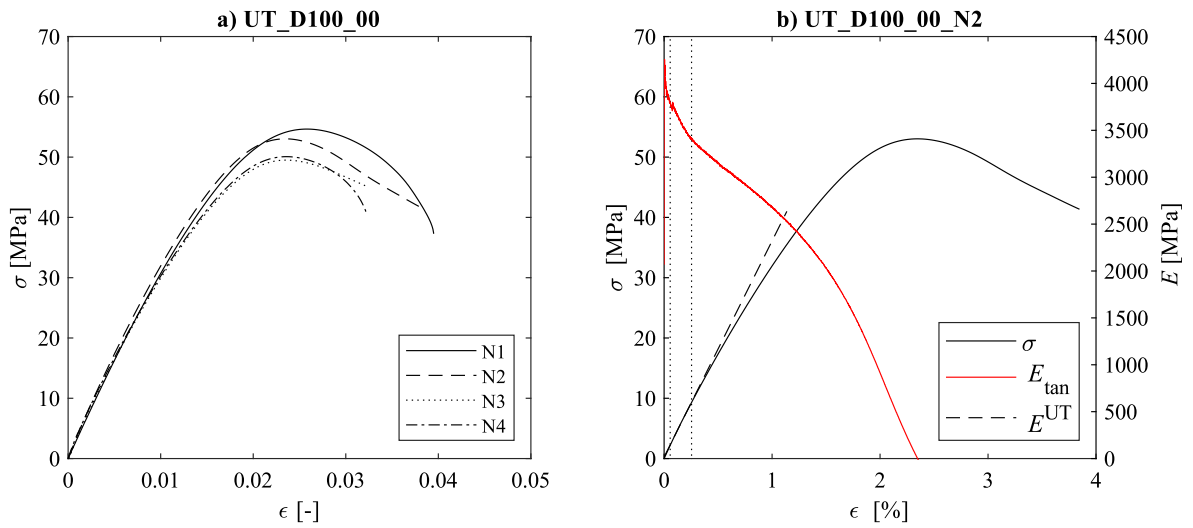$$L_c = \frac{1}{\pi}\left(\frac{K_c}{\sigma_o}\right)^2 \tag{6}$$

Fig. 9. a) Nominal stress against nominal strain for dog-bone specimens under UT test. b) Instantaneous tangent elastic modulus of specimen UT_D100_00_N2 and resulting tensile elastic modulus E_{tan}.
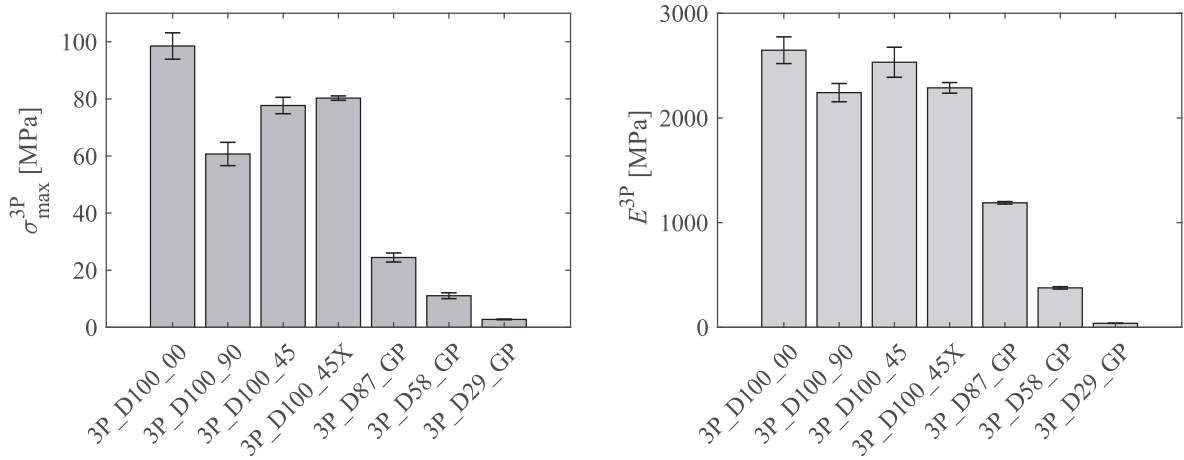

Fig. 10. Mean experimental σ_{max}^{3P} (left) and E^{3P} (right) for prismatic specimens tested under 3P bending.

TCD will be applied to predict failure in GP specimen models (3P_D29_GP, 3P_D58_GP and 3P_D87_GP), requiring K_c of PLA and the estimation of the characteristic material parameters σ_o and L_c (in Section 3.3).

3. Results

Three subsections including results from uniaxial tensile tests, three-point bending tests and the static strength assessment using the TCD in the GP specimens are presented in this section.

3.1. Uniaxial tensile tests

Dog-bone specimens (UT_D100_00) were tested under UT loading (description of the procedure in Section 2.2.1). The displacement field tracked through the DIC technique and the strain measured by the extensometer were used to calculate the mean values of Poisson's ratio ν and tensile elastic modulus E^{UT}, being 0.38 and 3.66 GPa, respectively. In addition, the nominal tensile strength at yield σ_y was obtained from the experimental force-displacement curves, with the mean value of 53 MPa.

Fig. 9 shows the nominal stress-strain curves for dog-bone specimens measured by the clip-on extensometer (Fig. 9a) and the stress-strain curve for specimen UT_D100_00_N2 with the instantaneous tangent modulus of elasticity E_{tan} (Fig. 9b). We can observe a quasi-linear relationship at the beginning of the test corresponding to the elastic region. However, E_{tan} shows a significant decrease even at very low deformations (vertical dotted lines define the region recommended by ISO 527 [48,49] where E^{UT} is calculated between
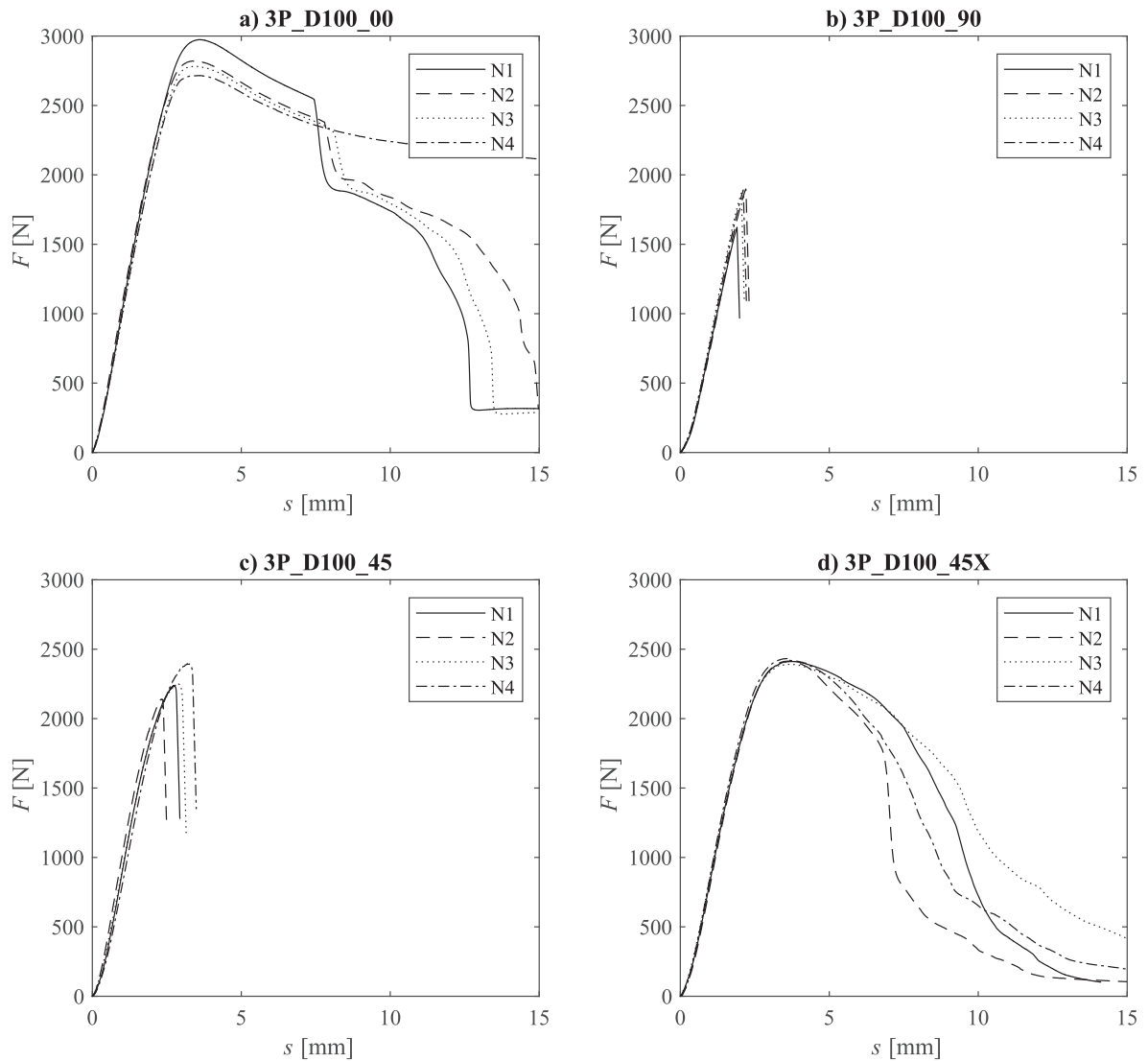
Fig. 11. Force-displacement curves of fully dense specimens under 3P bending test.

0.05% and 0.25% as the average of E_{tan}). We can conclude that the material does not exhibit a Hookean behaviour. As it can be seen, the maximum nominal stress is approximately achieved at 0.025 strain, just prior to necking.

The specimen is prone to develop a neck which may get stable and travels along the specimen. The necking phenomenon in rigid polymers mainly causes a decrease of the stress-strain slope followed by a strain-hardening [55–57]. Thermal effects in polymers usually cannot be neglected, and they are known to produce a mechanical softening. Nevertheless, the crosshead speed utilised in this work was significantly low to assume an isothermal process. The initiation of the neck started at some part of the specimen where the cross-sectional area is subjected to high stress. It can be produced due to a stress concentration such as at the corner radius or a manufacturing defect along the middle section.

3.2. Three-point bending tests

Prismatic specimens were tested under 3P bending (description of the procedure in Section 2.2.1). The mechanical behaviour of these samples is analyzed considering both global and local approaches, from the overall mechanical properties to the effects of the process parameters on the 3D printed structure. Moreover, a fracture morphology study is carried out.

3.2.1. Global mechanical behaviour

Table 4 (see appendix) shows the results of each specimen design obtained in the 3P bending tests. In particular, the variables included are maximum force F_{max}, flexural stiffness K, flexural strength σ_{max}^{3P} and flexural elastic modulus E^{3P}. Note that the
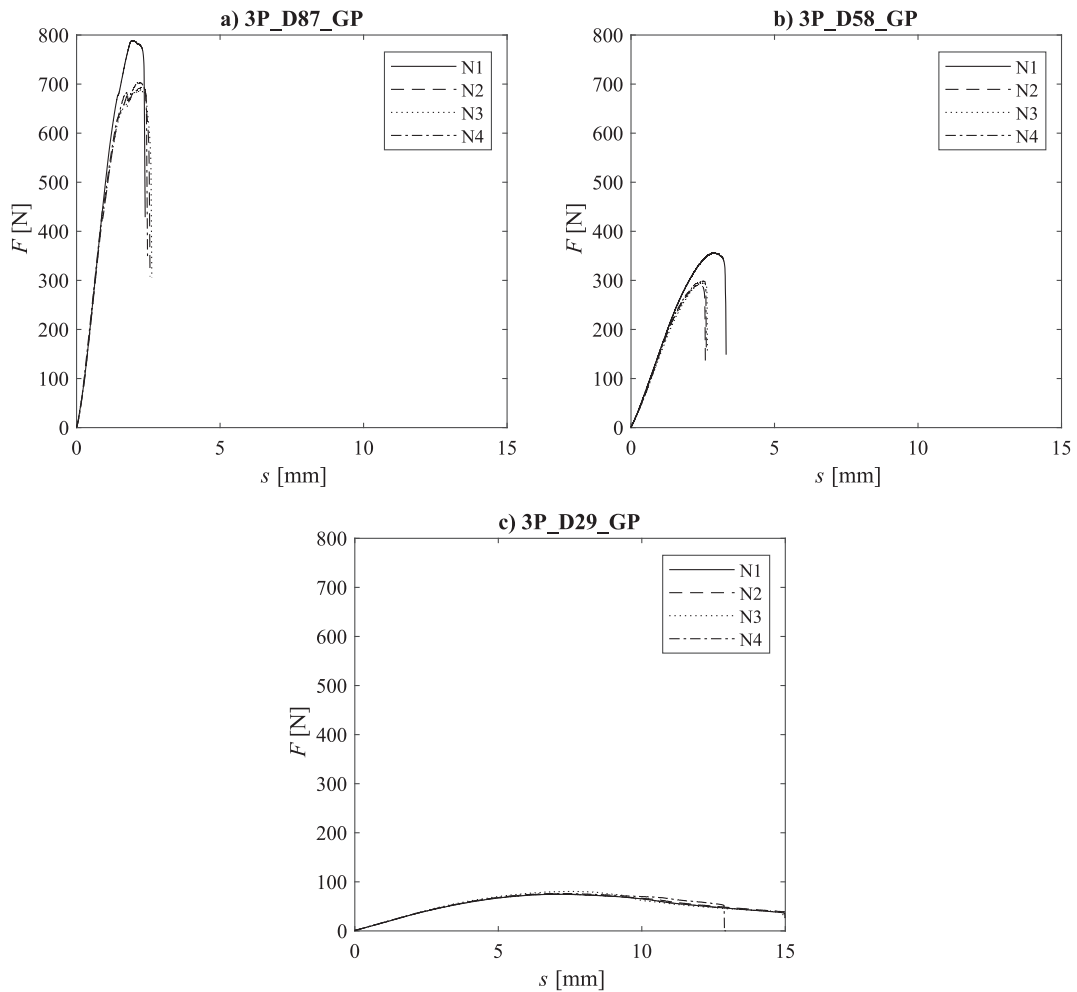
Fig. 12. Force-displacement curves of GP specimens under 3P bending test.

corresponding σ_{max}^{3P} and E^{3P} were analytically calculated from the experimental K and F_{max} using Eqs. (1) and (5), respectively.

Fig. 10 plots in a bar graph the mean and standard deviation of the experimental results listed in Table 4 for each specimen configuration in terms of σ_{max}^{3P} and E^{3P}. Figs. 11 and 12 represent the force-displacement curves obtained during tests for fully dense and GP specimens, respectively.

Regarding fully dense specimens, geometry and density percentage remain constant and raster orientation becomes the key factor. Now all samples reach the σ_{max}^{3P} about the same order of magnitude and present a similar E^{3P} (see Fig. 10). Nevertheless, it is worth noting that 3P_D100_00 is slightly better in terms of mechanical properties. Conversely, 3P_D100_90 is below of the rest. However, the main differences in this type of specimens rely on the failure mechanism, as shown in Fig. 11. Note that 3P_D100_90 and 3P_D100_45 exhibit a brittle fracture at a certain deflection. By contrast, 3P_D100_00 and 3P_D100_45X tend to a ductile behaviour when failure initiates, reaching large elongations before the total loss of their strength.

For GP specimens, it is obvious to conclude that the higher the infill density, the higher the F_{max}, K and thus E^{3P} (see Figs. 10 and 12). Samples with higher densities (3P_D58_GP and 3P_D87_GP) exhibit a brittle response once the F_{max} is reached. By contrast, specimen 3P_D29_GP presents a great elongation as its strength gradually decreases until total fracture, as represented in Fig. 12. Note that 3P_D29_GP sample is less constrained than 3P_D58_GP and 3P_D87_GP specimens. This has been demonstrated useful to control brittleness in materials.

3.2.2. Local mechanical behaviour

Fig. 13 shows the maximum principal Lagrangian strain field for four different fully dense specimens prior to failure where the influence of the raster orientation on the strain field can be clearly observed. It is quite easy to recognise the different printing angles in all specimens but 3P_D100_00, which will be discussed below. Notice that the measured maximum principal strain concentrates at the interface between two adjacent strands (intra-layer bond, see Fig. 1), and not on the strand itself. In addition, it is remarkable that sample 3P_D100_90 abruptly fails at a relatively low strain (note the different scales used in Fig. 14), but enough to appreciate the
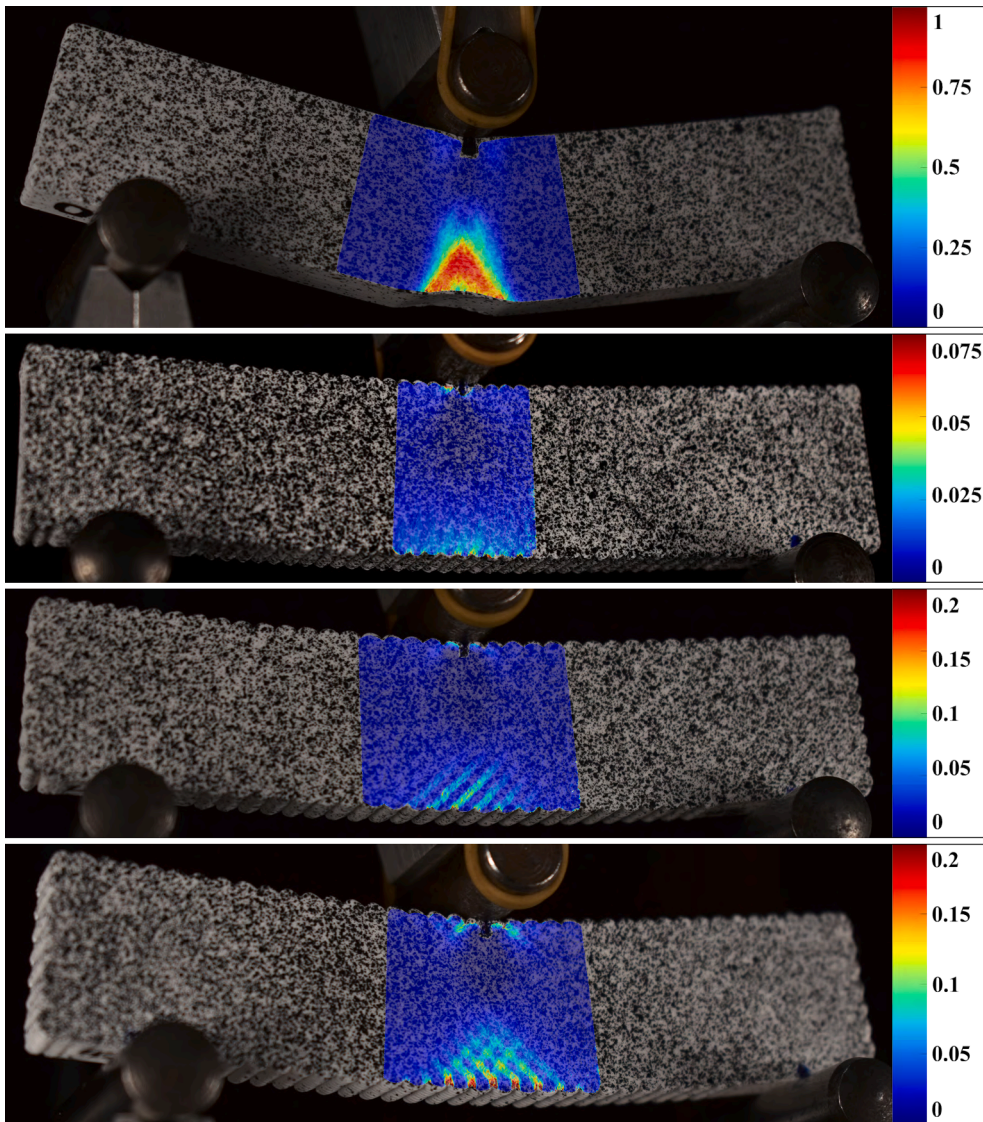
Fig. 13. Maximum principal Lagrangian strain field for fully dense specimens under flexural loading at maximum load obtained through DIC technique. From top to bottom: 3P_D100_00, 3P_D100_90, 3P_D100_45 and 3P_D100_45X.

stress concentration produced at each intra-layer bond.

Fig. 14 shows the measured principal Lagrangian strain field at instants close to the maximum force to assess the strain field evolution for specimen 3P_D100_00_N1. The maximum principal Lagrangian strain started at the bottom face of the specimen for the test condition 3P_D100_00 (see Fig. 14b left side). The strain field is similar to the predicted by the Euler-Bernoulli beam theory at this early stage presenting a homogenous distribution. The phenomenon seems similar to the neck formation in the UT test where the normal section is drastically reduced and the shoulders travel along the specimen. However, due to the compressive stresses at the top side and the contact loads, specimen thickening appears at the top face of the specimen. In this way, the shoulders of the neck travel only up to the neutral axis and then move laterally in test condition 3P_D100_00.

Note that DIC technique could not be applied to GP specimens due to the small thickness of the lattice structure (approximately 1 mm), with this technique is significantly difficult to obtain accurate results with our setup, considering pixel size, speckle pattern and camera optics.. The DIC processing in GP samples with such a speckle resulted in excessive noise, precluding accurate measurements.

3.2.3. Fracture morphology assessment

Fracture morphology analysis usually reveals essential information to determine the cause of mechanical failure. This subsection presents the macro-fracture surfaces orientation or crack trajectories of fully dense and GP specimens.

Fig. 15 shows the front view of the fracture pattern orientation in fully dense specimens. As it can be seen, planar cracks were generally led by the raster orientation through the intra-layer bonds, except for 3P_D100_00 where the macro-crack grows
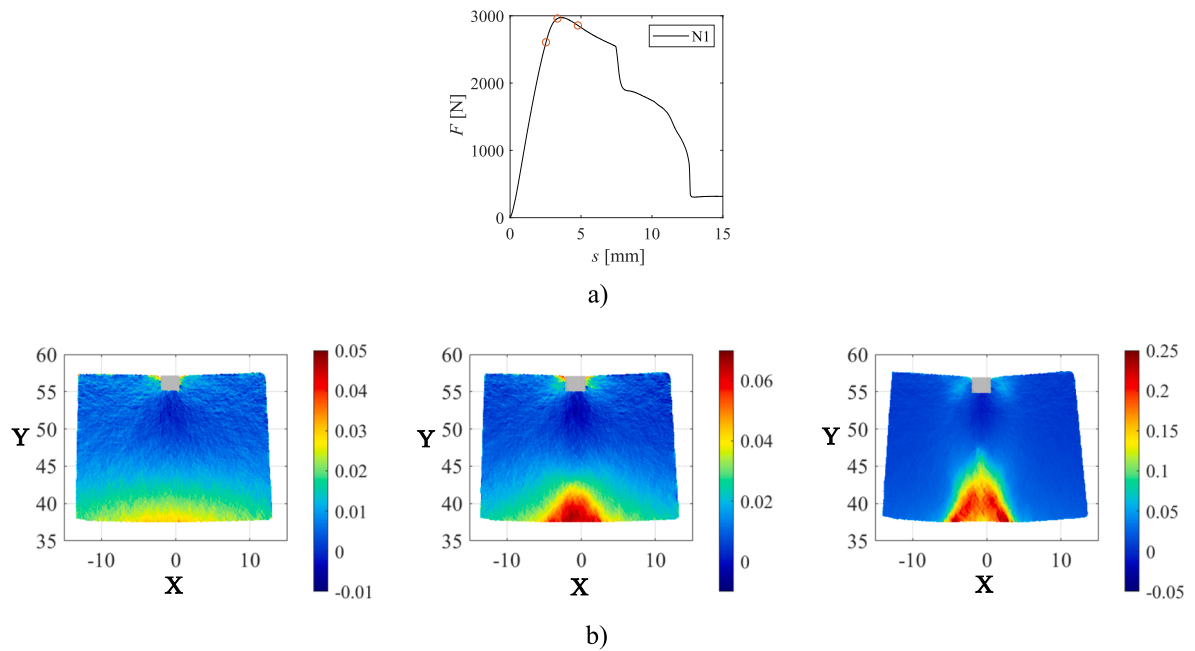
a)

b)

Fig. 14. a) Force-displacement curve for specimen 3P_D100_00_N1. b) Maximum principal Lagrangian strain fields for specimen 3P_D100_00_N1 under flexural loading obtained through DIC at the three instants marked with red circles at force-displacement curve. The marks for alignment of the specimens resulted in untracked areas represented by grey rectangles on the strain fields. (For interpretation of the references to colour in this figure legend, the reader is referred to the web version of this article.)
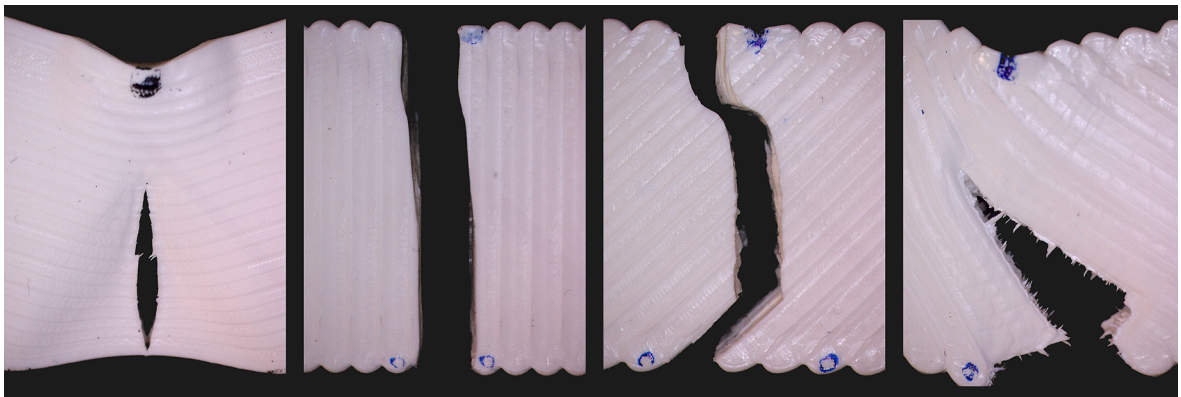

Fig. 15. Post-failure captures at the middle section in fully dense specimens under 3P bending test. From left to right: 3P_D100_00, 3P_D100_90, 3P_D100_45 and 3P_D100_45X (blue top dot indicates the location of upper pin). (For interpretation of the references to colour in this figure legend, the reader is referred to the web version of this article.)

perpendicular to this direction.

Cracks were usually initiated at the bottom face of the specimen except from 3P_D100_00, where significant ductility was found, and the crack initiated close to the neutral axis (see Fig. 16a). Specimens were observed during experiments by means of a portable microscope. It was only possible to observe the crack propagation at the surface of the specimen with the microscope for test conditions 3P_D100_00 and 3P_D100_45X, because 3P_D100_90 and 3P_D100_45 failed in a brittle manner, and it was not possible to capture the rapid crack propagation process. For 3P_D100_00 and 3P_D100_45X, the crack started at the inner region of the specimen because a significant drop of the measured force was always found before observing the surface cracks with the microscope. However, we were able to observe that a micro-crack usually tends to initiate between two adjacent strands at the intra-layer region (see Fig. 16a and Fig. 17a). As crack grows, the crack surface kinks toward an orientation normal to the extension stress direction (see Fig. 16d and Fig. 17d). As shown in Fig. 17, a zigzag crack trajectory was found in 3P_D100_45X. Moreover, in some cases, multiple symmetric micro-cracks initiated, although one main macro-crack was always observed in all cases at the end of the tests.

Regarding the specimens manufactured with a GP, crack trajectories are depicted in Fig. 18. Fig. 18b shows a significant
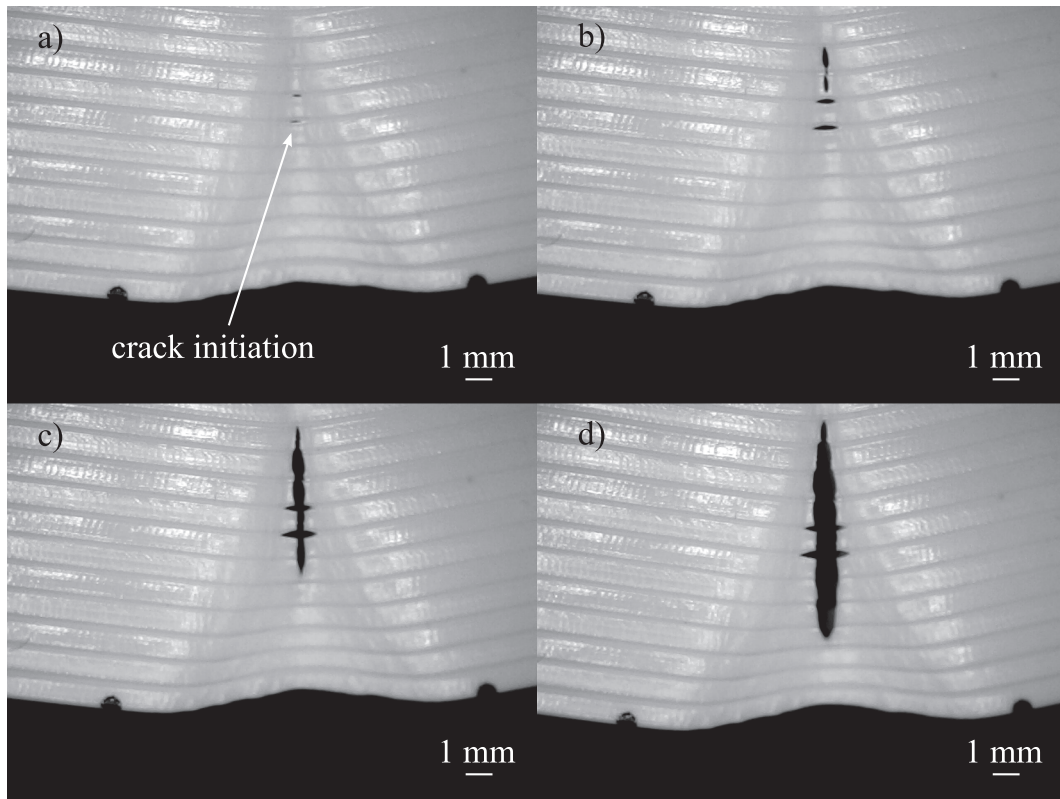
Fig. 16. Front view of crack nucleation and growth at the bottom face of specimen 3P_D100_00_N2. Pictures obtained from a portable optical microscope during the tests.

repeatability for most test conditions. Cracks propagate preferentially around the knot in a zigzag manner. Note that for the 3P_D29_GP test condition, only one specimen completely failed and only one path (N4) is shown in Fig. 18b. Furthermore, crack initiation sites in 3P_D29_GP and 3P_D58_GP test conditions were not located in the central section. This deviation is caused by a specific printing defect and will be explained in detail in Section 4.

3.3. Numerical results: Static strength assessment

This subsection provides the results of the FEA and the application of the TCD to GP specimens. First of all, the experimental initial slope of the deflection vs force response (i.e., the 3P bending stiffness) was compared to the FE estimated response to validate the material model for the simulation of PLA GP specimens. The calculated values and relative errors between the numerical and experimental stiffness are listed in Table 5. The calculated values and relative errors between experimental and numerical results are listed in the following table. We consider that the average relative error falls within the limits of the deviation of our results. However, we can see that the maximum relative error was obtained for the specimen configuration that experimentally presented a ductile behaviour (3P_D29_GP) and geometrical nonlinearity.

The maximum principal stress field at the instant of mean experimental maximum force (see Table 6) is shown in Fig. 19 for the GP models (3P_D29_GP, 3P_D58_GP and 3P_D87_GP). Hot spots are located on the connective links of the lattice structure under significant stress gradients. In particular, the central bottom knot of each geometry is analysed as the predicted critical location where the crack will be initiated by tensile loading (critical regions magnified in Fig. 19).

As stated in Section 2.3, TCD was implemented to predict crack nucleation in GP numerical models using the point method approach through Equation (6). Firstly, considering plane strain conditions due to model specifications, K_c for PLA was taken as 3.7 MPa·m$^{1/2}$ [14]. Then, σ_o was considered to be correlated with the mean value of σ_{max}^{3P} for 3P_D100_00 specimens, resulting σ_o equal to 98.56 MPa. Finally, according to the expression that defines the critical distance L_c, Equation (6), this parameter is 0.448 mm and $L_c/2$ is 0.224 mm. Following TCD, knowing σ_o and the load applied at a certain crosshead displacement with the generated stress at $L_c/2$ from the notch tip, it is simple to estimate the numerical F_{max} at which the failure will occur.

According to the simulations, applied loads required to cause failure nucleation are indicated in Table 6, as well as the comparison with the experimental results. Note that the predicted values are greater than experimental results. The growth of the crack path across the adjacent upper joints completes the modelled fracture.
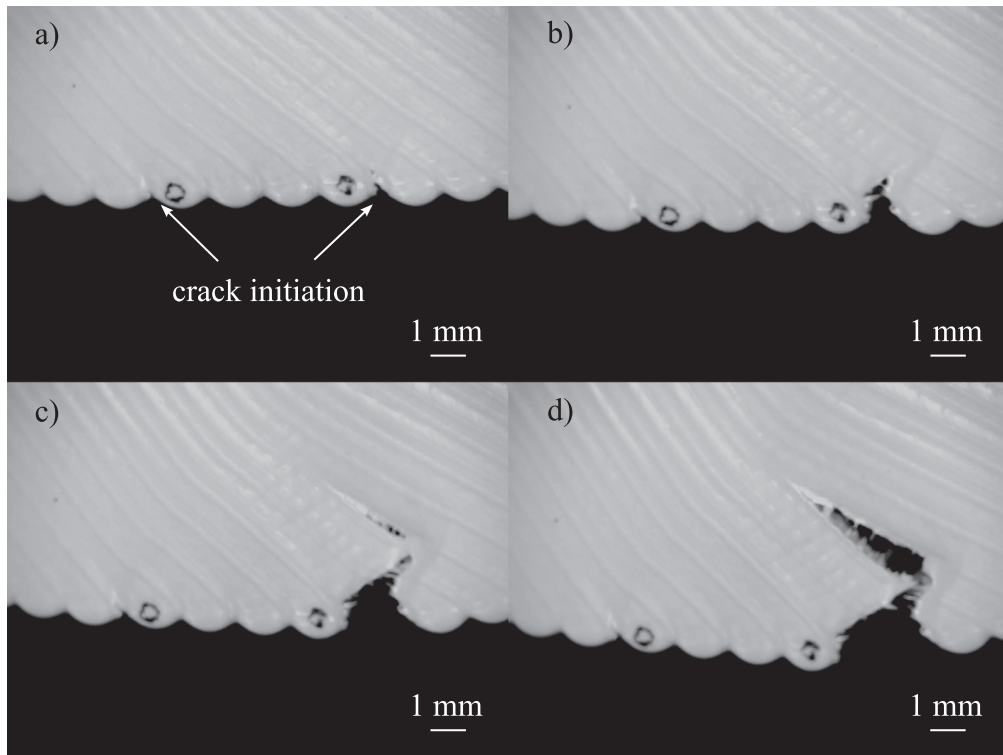
Fig. 17. Front view of crack nucleation and growth at the bottom face of specimen 3P_D100_45X_N4. Pictures obtained from a portable optical microscope during the tests.

4. Discussion

Regarding the mechanical properties obtained of PLA, measured E^{UT} is in line with previous research works [12–15]. Additionally, the measured ν and σ_y agree well with the values obtained by Ferreira et al. [58] for 0° raster orientation.

In order to analyse the impact of different process parameters, it is necessary to assess the prismatic samples separately. In the case of fully dense specimens, the influence of the raster orientation on the experimental results will be assessed. As mentioned in Section 3.2.1, specimens with 90° raster orientation (3P_D100_90) were significantly weaker than the other test conditions in terms of mechanical properties (see Fig. 10). By contrast, specimens with 0° raster orientation (3P_D100_00) were slightly ahead, reaching the maximum measured properties listed in Table 4. Note that although the air-gap value was set to negative, the raster orientation still showed a significant large influence on the strength. These outcomes correlate with the investigations by Ahn et al. [31] and Khosravani et al. [59], testing these configurations under tensile loading.

On the other hand, the study for GP specimens should focus on the effect of the infill density on the mechanical behaviour. As density increases, lattice dimensions are reduced and the structure is more constrained, thus, affecting failure conditions. Reported by Taylor [60], a less constrained sample often leads to a ductile response (3P_D29_GP) and, conversely, more constrained parts are prone to abrupt fractures (3P_D58_GP and 3P_D87_GP). These results are in line with the results presented by Fernández-Vicente et al. [61] where increasing the infill density leads to higher stresses, but a lower degree of deformation. These statements can be applied to explain the global mechanical behaviour for this infill pattern.

The ultimate mechanical properties of the deposited strand, inter-layer and intra-layer bonds may differ and they are function of the process parameters (e.g. air gap and layer thickness) and the thermal properties such as thermal history of the feedstock [41,62]. As shown in Fig. 13, the maximum strain field concentrates on the intra-layer bonds of fully dense specimens. These regions seem to present a lower strength (bottom face of the sample during bending) and their assessment becomes crucial to understand the mechanical behaviour of the whole 3D printed geometry. Stated by Özen et al. [63], one of the most critical factors affecting the mechanical properties of MEX parts is the molecular diffusion in the inter-layer and intra-layer bonds (influenced by the aforementioned variables). In addition, larger contact areas between two adjacent strands lead to a better diffusion of the material. Therefore, porosity in fully dense specimens generates weak interfaces introducing voids and stress raisers into the structure, causing a brittle failure [63–65]. This may justify the abrupt fracture obtained for 3P_D100_45 and 3P_D100_90 (see Fig. 11b and 11c), where the intra-layer bonds are subjected to most part or all of the load, respectively. This behaviour in contrast to the ductile response of 3P_D100_00 and 3P_D100_45X (see Fig. 11a and 11d), where the load is completely or partially applied on the strands, respectively.

It is well known that the failure of amorphous and semi-amorphous polymers starts at the micro-scale with the shear band formation or the shear yielding and the crazing phenomena (i.e., the generation of microscopic voids), which further develop into main
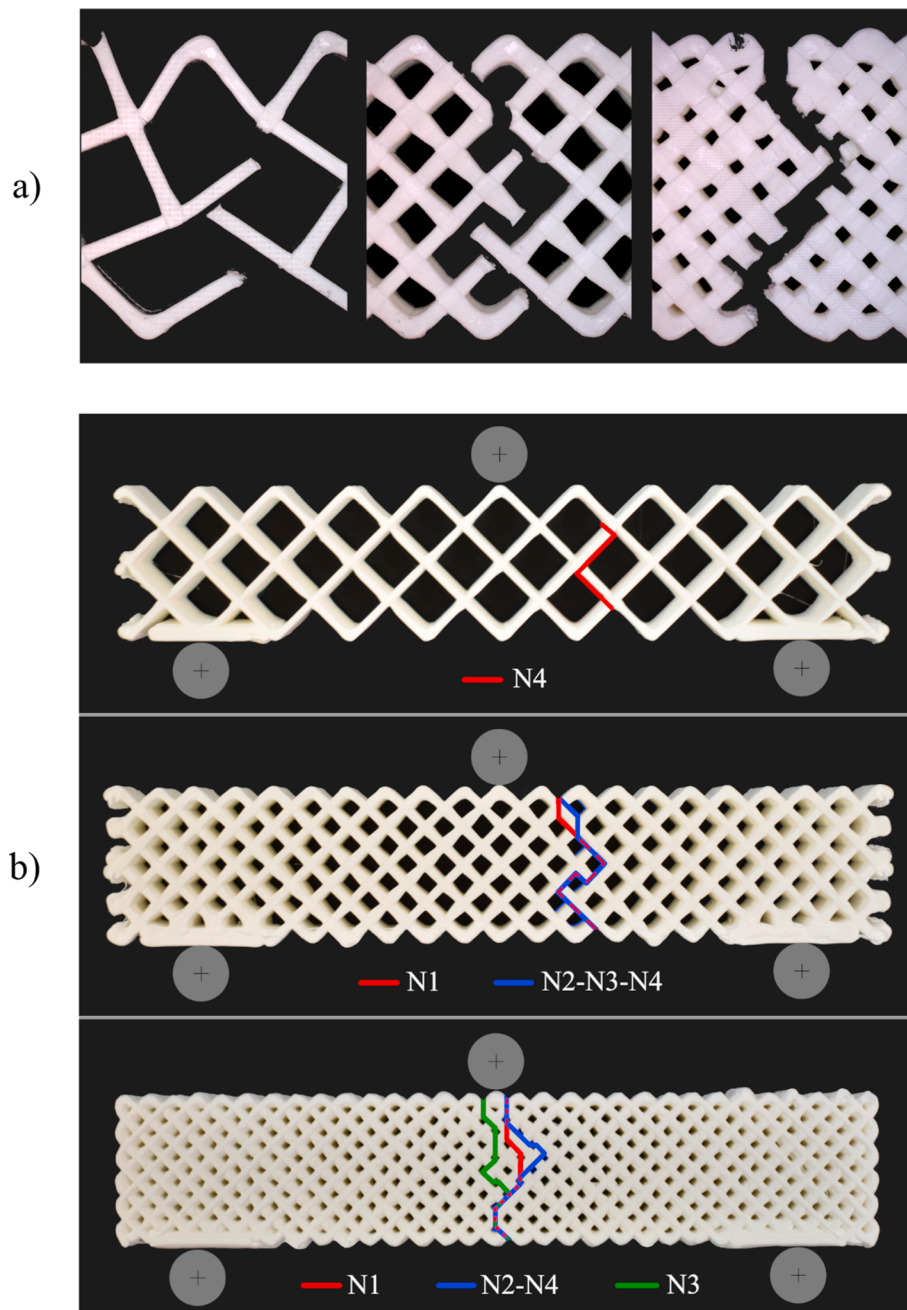
Fig. 18. a) Fracture patterns and b) crack path repeatability for GP specimens under 3P bending test. From left to right and top to bottom: 3P_D29_GP, 3P_D58_GP and 3P_D87_GP.

Table 5
Relative error between the numerical FEA stiffness and the experimental stiffness of the GP specimens.

Specimen	Numerical Stiff. [N/mm]	Experimental Stiff. [N/mm]	Error [%]
3P_D29_GP	20.93	16.50	26.85
3P_D58_GP	182.75	164.64	11.00
3P_D87_GP	579.05	550.40	5.20

Table 6

Mean experimental and predicted F_{max} for GP test conditions under 3P bending test with the corresponding relative errors.

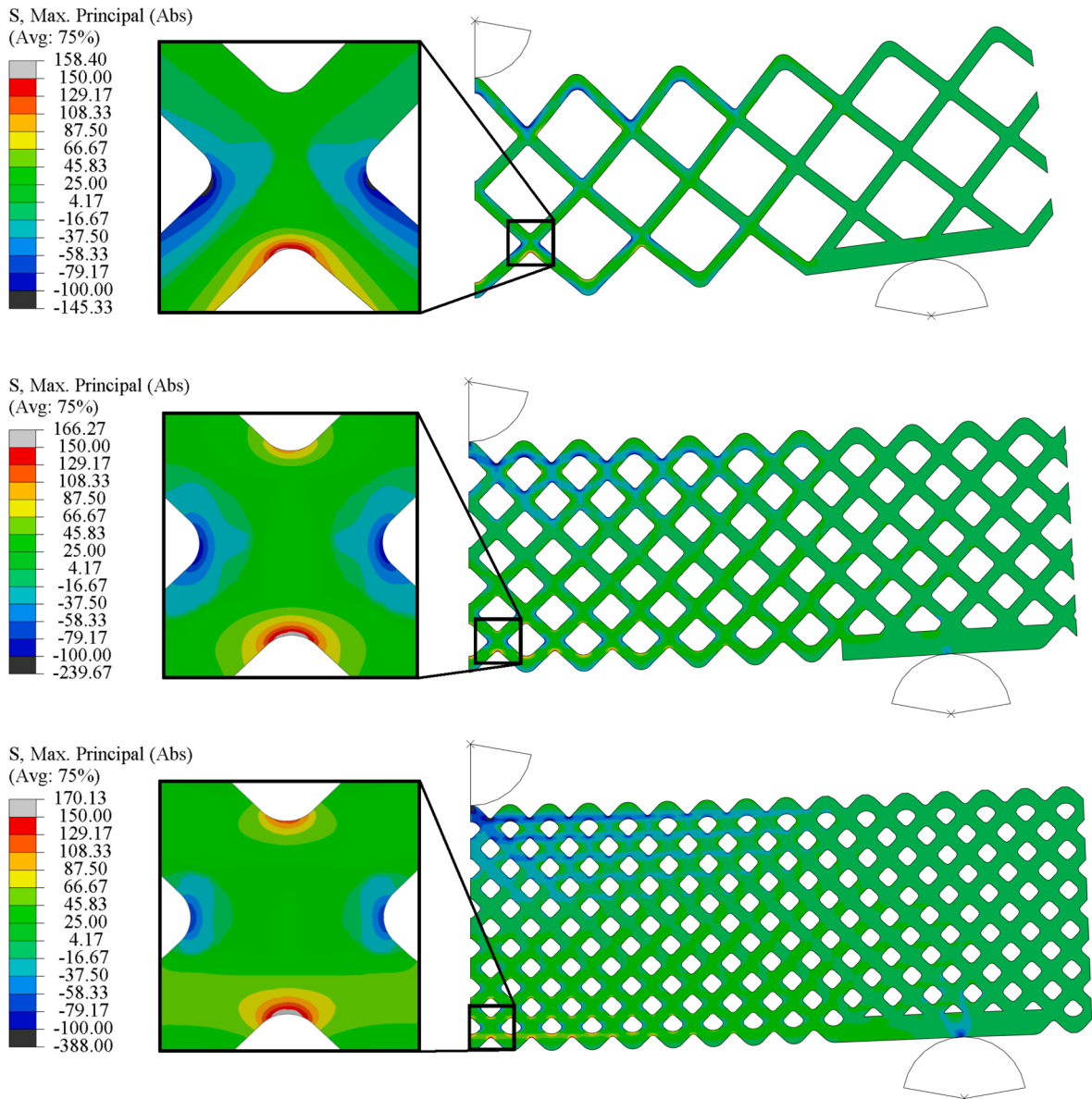| Specimen	F_{max} [N]		Error [%]
	Experimental	Predicted	
3P_D87_GP	718.32	1073.77	49.48
3P_D58_GP	310.39	559.50	80.26
3P_D29_GP	76.66	145.82	90.22

Fig. 19. Maximum principal stress distribution in MPa of GP numerical models under 3P bending at experimental failure. From top to bottom: 3P_D29_GP, 3P_D58_GP and 3P_D87_GP.

developed cracks [66,67]. These cracks usually show small fibrils spanning their faces [68].

After the observation of the DIC results, the crazing phenomenon is likely to be located along the large voids that act as stress raisers which are naturally generated between filament/layers in MEX [17]. In our work, these bands of large strain concentration are located close to the central bottom face of the 3P bending specimen, and following the feedstock material deposition angle (see Fig. 13). Note that in this work the specimens were made with a negative air gap which is usually responsible to reduce the generation of large voids
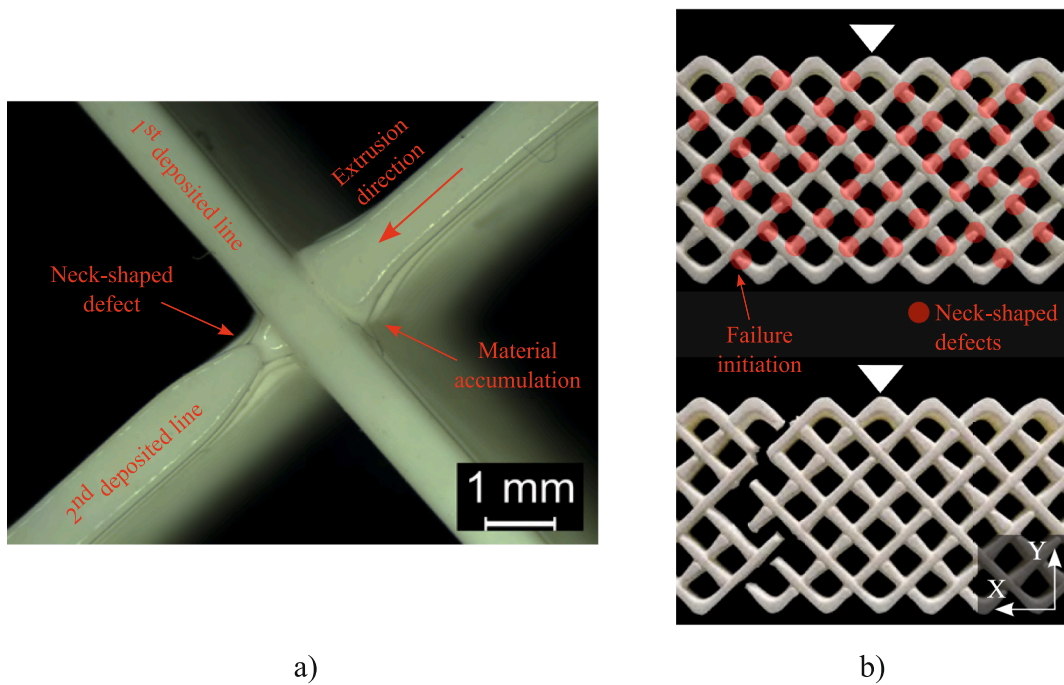
Fig. 20. a) Bottom view of a knot in the lattice structure and b) influence of neck-shaped defects (highlighted in red) on crack trajectory in specimen 3P_D58_GP_N3 before (top) and after (bottom) fracture. (For interpretation of the references to colour in this figure legend, the reader is referred to the web version of this article.)
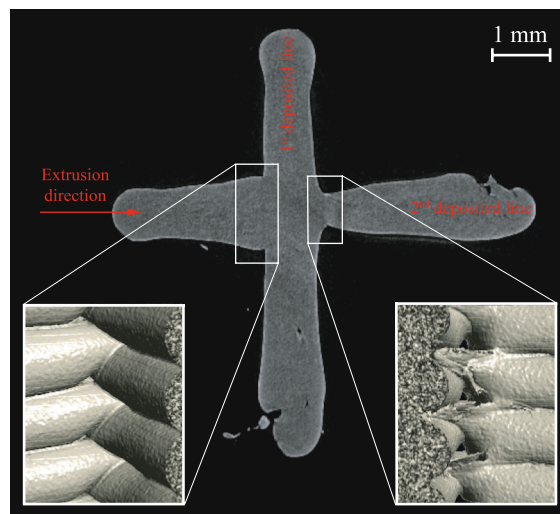

Fig. 21. Micro-CT scan for cross-shaped sample. Reconstructed 3D geometries of grid joint: details for the strong bond (left side) and weak bond with neck-shaped defect (right side).

between strands [31,35–37]. Nevertheless, the phenomenon was still clearly observed.

On the other hand, linking fibrils are not observed when the crack is aligned with bonding planes (see Fig. 15). This allows for a more rapid fracture (i.e., a brittle fracture behaviour). However, in some cases the energy available at the crack tip is not enough to generate new surfaces at the weak bonding planes. Thus, the crack propagates through the cross-layer plane (see Figs. 16 and 17) in which the fibrils can be observed. Therefore, a more ductile fracture response was presented [18]. In summary, the failure mechanism is mainly driven by two factors: 1) the location and orientation of geometric features that act as stress-raisers (i.e., the large voids generated during the deposition between adjacent strands); 2) the inter-layer and intra-layer weak interfaces due to thermal effects [41,62].

Concerning the fracture patterns obtained for fully dense specimens (see Fig. 15), all test conditions correlate to previous works

[31,59]. The crack growth is significantly dependent on the raster orientation, tending to a propagation normal to the top face of the sample through intra-layer bonds. In the case of 3P_D100_45X, the fracture pattern followed a zigzag trajectory alternating strands and intra-layer bonds from different layers, as reported in the aforementioned work by Ahn et al. [31]. The results are in line with the fracture pattern obtained by Ayatollahi et al. [38]. The same investigations confirm that this dependence on the raster orientation is not applicable to 3P_D100_00, in which the main crack propagated through deposited strands, although some initial crack was observed in the intra-layer region. On the other hand, fracture morphology for GP specimens is based on the assessment of breakage around joints (see Fig. 18a). An off-center crack initiation for 3P_D58_GP and 3P_D29_GP during experimental tests, which was unexpected from numerical models, can be justified by a specific printing defect to be discussed below.

The study of the GP manufacturing is carried out to find the cause of the disagreement between the experimental and predicted results in the fracture patterns and static strength. Note that during printing, the filament is deposited twice in each knot of the lattice structure for each layer, resulting in a priori accumulation of extruded material in the knot (i.e., the extruder head passes twice through each knot). Fig. 20a shows an optical microscopy picture of the bottom view in a knot of a GP specimen. As it can be seen, the 2nd deposited line presents an irregular shape close to the knot. Due to the previous deposited line, there is an inconsistent extrusion after passing this joint in which appears a neck-shaped defect. This implies material accumulation in one side of the cross-joint, and shortage in the other. Fig. 20b proves the significance of the neck-shaped defect in GP specimens by the presence of one weak bond in each knot. As shown in Fig. 20b, the fracture initiates on the nearest neck-shaped defect to the centre which is located on the bottom part of the knot (highlighted in Fig. 20b with red circles). Next, the fracture keeps growing along the neck-shaped defects. Note that the fracture pattern repeatability was significantly high as shown previously in Fig. 18b.

In order to analyse this defect in detail, a cross-shaped sample was fabricated to simulate one of these joints. This sample was 3D scanned using the micro computed tomography (micro-CT) scanner Bruker Skyscan 1172, with 40 kV of voltage, 250 μA of current, 9 μm of camera pixel size and 580 ms of exposure time. Fig. 21 shows the section of the sample through the middle of an arbitrary layer. Note that the vertical line was deposited first, and then the horizontal one from left to right. The accumulation of extruded material on the left side of the joint is considerably high, creating a wider bond with a homogeneous diffusion (see Fig. 21 left side). By contrast, on the right side, the generated section is significantly thinner when the nozzle passes through the first strand. Fig. 21 right side represents the side view of the weak bond with voids caused by the lack of material, comparable to the bonding problems reported by Webbe et al. [34] and the generation of stress raisers stated by Allum [17] during the filament deposition. However, in this case, the geometric neck-shaped feature due to the lack of material is the responsible of driving the premature failure of these knots, rather than a bonding problem due to diffusion of the material between adjacent strands. This defect is considered enough to advance breakage in GP specimens. We observed that the fracture pattern was preferentially gone through the neck-shaped defect (side with material shortage), especially at early fracture stages (see Fig. 20b). Moreover, the great repeatability in the fracture pattern (see Fig. 18b) shows that this defect mainly dominates the failure location and propagation. Note that depending on the extruder path direction the crack will change its trajectory, and this should be considered for optimization of the mechanical behaviour.

5. Conclusions

In this work, a complete fracture assessment of 3D printed specimens by means of MEX-based additive manufacturing has been carried out. The research includes experimental testing with DIC technique and numerical modelling. The main conclusions drawn from this work are:

- This study demonstrates that geometric features such as the large voids generated between strands in fully dense specimens and the neck-shaped defect in GP samples are mainly responsible of the failure mechanism of MEX PLA components.
- When the crack propagates through cross-strand planes, the fracture behaviour is ductile. However, a transition from ductile to brittle behaviour is present in specimens when changing the raster orientation to the loading axis (i.e., when the crack starts to grow through intra-layer bond planes).
- The raster orientation significantly influences the failure mechanism in fully dense specimens under 3P bending because it further controls the orientation of the geometric defects and the weak inter-layer bonding planes.
- Because the GP specimens tend to fail at joints due to a neck-shaped defect close to the stress raisers, the location of the defect in the knot is affected by the nozzle path direction. Therefore, we demonstrate not only the importance of the GP infill itself but also of the deposition nozzle path, which is generated by the slicer software.
- The commercial AM software used in this work generates the deposition path according to internal algorithms that cannot be controlled by the user. However, this has a critical effect on the failure behaviour, as shown in our study. As the mechanical behaviour of the AM part is of utmost importance in practice, an in-depth research is still missing in the literature that relates the path deposition algorithm with the final mechanical behaviour.
- TCD estimations in GP specimens were significantly non-conservative because the numerical model did not include the neck-shaped defect. In fact, the differences found in the TCD analysis motivated the in-depth study of the joints, allowing the discovery of the neck-shaped defect with CT-scans. This illustrates the importance of numerical predictive tools along with experimental observations when analysing failure analysis.
- A non-homogeneous distribution of the strain field was measured thanks to the DIC technique. The largest strains were located in the areas between two adjacent strands. In this way, we demonstrate that fully dense specimens cannot be considered isotropic solids under 3P bending loading. This is due to the geometric features that naturally appear during the material extrusion and deposition process.

Table 4
Experimental results for prismatic specimens tested under 3P bending.

Test	F_{max} [N]	σ_{max}^{3P} [MPa]	K [N/mm]	E^{3P} [MPa]
3P_D100_00_N1	2973.70	104.11	1221.05	2629.44
3P_D100_00_N2	2819.99	99.71	1223.45	2634.62
3P_D100_00_N3	2781.10	97.37	1144.86	2468.08
3P_D100_00_N4	2715.64	93.03	1151.12	2511.12
3P_D100_90_N1	1621.74	54.59	1004.49	2278.98
3P_D100_90_N2	1897.56	62.81	1084.11	2489.25
3P_D100_90_N3	1866.68	62.98	1105.67	2538.76
3P_D100_90_N4	1889.55	62.39	1079.71	2479.17
3P_D100_45_N1	2235.28	77.66	1190.22	2769.34
3P_D100_45_N2	2141.07	74.38	1211.29	2818.36
3P_D100_45_N3	2250.31	77.25	1126.86	2653.89
3P_D100_45_N4	2394.23	81.39	1099.81	2558.99
3P_D100_45X_N1	2411.55	79.63	1084.47	2428.27
3P_D100_45X_N2	2414.25	80.49	1086.99	2466.17
3P_D100_45X_N3	2391.39	79.73	1076.52	2410.47
3P_D100_45X_N4	2432.13	81.28	1125.48	2458.07
3P_D87_GP_N1	788.02	26.79	559.90	1190.31
3P_D87_GP_N2	693.66	23.58	548.39	1135.77
3P_D87_GP_N3	688.41	23.35	547.39	1162.79
3P_D87_GP_N4	703.18	24.14	545.92	1131.39
3P_D58_GP_N1	356.16	12.59	164.34	362.81
3P_D58_GP_N2	291.78	10.44	165.53	365.44
3P_D58_GP_N3	294.98	10.56	158.43	345.62
3P_D58_GP_N4	298.63	10.69	170.25	366.62
3P_D29_GP_N1	74.67	2.70	16.27	33.71
3P_D29_GP_N2	75.22	2.72	16.55	34.73
3P_D29_GP_N3	80.49	2.94	16.66	34.96
3P_D29_GP_N4	76.24	2.76	16.50	34.61

Declaration of Competing Interest

The authors declare that they have no known competing financial interests or personal relationships that could have appeared to influence the work reported in this paper.

Data availability

Data will be made available on request.

Acknowledgements

Appendix

See Table 4.

References

[1] Culmone C, Smit G, Breedveld P. Additive manufacturing of medical instruments: A state-of-the-art review. Addit Manuf 2019;27:461–73. https://doi.org/10.1016/j.addma.2019.03.015.

[2] Altıparmak SC, Xiao B. A market assessment of additive manufacturing potential for the aerospace industry. J Manuf Process 2021;68:728–38. https://doi.org/10.1016/j.jmapro.2021.05.072.

[3] Daminabo SC, Goel S, Grammatikos SA, Nezhad HY, Thakur VK. Fused deposition modeling-based additive manufacturing (3D printing): techniques for polymer material systems. Mater Today Chem 2020;16:23. https://doi.org/10.1016/j.mtchem.2020.100248.

[4] Song Y, Li Y, Song W, Yee K, Lee KY, Tagarielli VL. Measurements of the mechanical response of unidirectional 3D-printed PLA. Mater Des 2017;123:154–64. https://doi.org/10.1016/j.matdes.2017.03.051.

[5] Popescu D, Zapciu A, Amza C, Baciu F, Marinescu R. FDM process parameters influence over the mechanical properties of polymer specimens: A review. Polym Test 2018;69:157–66. https://doi.org/10.1016/j.polymertesting.2018.05.020.

[6] Fallon JJ, McKnight SH, Bortner MJ. Highly loaded fiber filled polymers for material extrusion: A review of current understanding. Addit Manuf 2019;30: 100810. https://doi.org/10.1016/j.addma.2019.100810.

[7] Das A, Chatham CA, Fallon JJ, Zawaski CE, Gilmer EL, Williams CB, et al. Current understanding and challenges in high temperature additive manufacturing of engineering thermoplastic polymers. Addit Manuf 2020;34:101218. https://doi.org/10.1016/j.addma.2020.101218.

[8] Wu H, Fahy WP, Kim S, Kim H, Zhao N, Pilato L, et al. Recent developments in polymers/polymer nanocomposites for additive manufacturing. Prog Mater Sci 2020;111. https://doi.org/10.1016/j.pmatsci.2020.100638.

[9] Goh GD, Yap YL, Tan HKJ, Sing SL, Goh GL, Yeong WY. Process–Structure–Properties in Polymer Additive Manufacturing via Material Extrusion: A Review. Crit Rev Solid State Mater Sci 2020;45:113–33. https://doi.org/10.1080/10408436.2018.1549977.

[10] Schnittker K, Arrieta E, Jimenez X, Espalin D, Wicker RB, Roberson DA. Integrating digital image correlation in mechanical testing for the materials characterization of big area additive manufacturing feedstock. Addit Manuf 2019;26:129–37. https://doi.org/10.1016/j.addma.2018.12.016.

[11] Ng CT, Susmel L. Notch static strength of additively manufactured acrylonitrile butadiene styrene (ABS). Addit Manuf 2020;34:101212. https://doi.org/10.1016/j.addma.2020.101212.

[12] Khosravani MR, Rezaei S, Ruan H, Reinicke T. Fracture behavior of anisotropic 3D-printed parts: Experiments and numerical simulations. J Mater Res Technol 2022;19:1260–70. https://doi.org/10.1016/j.jmrt.2022.05.068.

[13] Zhao Y, Chen Y, Zhou Y. Novel mechanical models of tensile strength and elastic property of FDM AM PLA materials: Experimental and theoretical analyses. Mater Des 2019;181:108089. https://doi.org/10.1016/j.matdes.2019.108089.

[14] Ahmed AA, Susmel L. A material length scale–based methodology to assess static strength of notched additively manufactured polylactide (PLA). Fatigue Fract Eng Mater Struct 2018;41:2071–98. https://doi.org/10.1111/ffe.12746.

[15] Ahmed AA, Susmel L. Static assessment of plain/notched polylactide (PLA) 3D-printed with different infill levels: Equivalent homogenised material concept and Theory of Critical Distances. Fatigue Fract Eng Mater Struct 2019;42:883–904. https://doi.org/10.1111/ffe.12958.

[16] Conway KM, Pataky GJ. Crazing in additively manufactured acrylonitrile butadiene styrene. Eng Fract Mech 2019;211:114–24. https://doi.org/10.1016/j.engfracmech.2019.02.020.

[17] Allum J, Gleadall A, Silberschmidt VV. Fracture of 3D-printed polymers: Crucial role of filament-scale geometric features. Eng Fract Mech 2020;224:106818. https://doi.org/10.1016/j.engfracmech.2019.106818.

[18] Lampron O, Lingua A, Therriault D, Lévesque M. Characterization of the non-isotropic tensile and fracture behavior of unidirectional polylactic acid parts manufactured by material extrusion. Addit Manuf 2023;61:103369. https://doi.org/10.1016/j.addma.2022.103369.

[19] Fayazbakhsh K, Movahedi M, Kalman J. The impact of defects on tensile properties of 3D printed parts manufactured by fused filament fabrication. Mater Today Commun 2019;18:140–8. https://doi.org/10.1016/j.mtcomm.2018.12.003.

[20] Baich L, Manogharan G, Marie H. Study of infill print design on production cost-time of 3D printed ABS parts. Int J Rapid Manuf 2015;5:308. https://doi.org/10.1504/IJRAPIDM.2015.074809.

[21] Hernandez R, Slaughter D, Whaley D, Tate J, Asiabanpour B. Analyzing the Tensile, Compressive, and Flexural Properties of 3D Printed Abs P430 Plastic Based on Printing Orientation Using Fused Deposition Modeling. In: 27th Annual International Solid Freeform Fabrication Symposium; 2016.

[22] Torres J, Cole M, Owji A, DeMastry Z, Gordon AP. An approach for mechanical property optimization of fused deposition modeling with polylactic acid via design of experiments. Rapid Prototyp J 2016;22:387–404. https://doi.org/10.1108/RPJ-07-2014-0083.

[23] Sood AK, Ohdar RK, Mahapatra SS. Parametric appraisal of mechanical property of fused deposition modelling processed parts. Mater Des 2010;31:287–95. https://doi.org/10.1016/J.MATDES.2009.06.016.

[24] Fatimatuzahraa AW, Farahaina B, Yusoff WAY. The effect of employing different raster orientations on the mechanical properties and microstructure of Fused Deposition Modeling parts, ISBEIA 2011 - 2011 IEEE Symposium on Business, Engineering and Industrial Applications; 2011, pp. 22–27. https://doi.org/10.1109/ISBEIA.2011.6088811.

[25] Durgun I, Ertan R. Experimental investigation of FDM process for improvement of mechanical properties and production cost. Rapid Prototyp J 2014;20: 228–35. https://doi.org/10.1108/RPJ-10-2012-0091.

[26] Ziemian C, Sharma M, Ziemian S. Anisotropic Mechanical Properties of ABS Parts Fabricated by Fused Deposition Modelling. Mech Engng 2012. https://doi.org/10.5772/34233.

[27] Ameri B, Taheri-Behrooz F, Aliha MRM. Mixed-mode tensile/shear fracture of the additively manufactured components under dynamic and static loads. Eng Fract Mech 2022;260:108185. https://doi.org/10.1016/j.engfracmech.2021.108185.

[28] Hart KR, Wetzel ED. Fracture behavior of additively manufactured acrylonitrile butadiene styrene (ABS) materials. Eng Fract Mech 2017;177:1–13. https://doi.org/10.1016/j.engfracmech.2017.03.028.

[29] Shanmugam V, Das O, Babu K, Marimuthu U, Veerasimman A, Johnson DJ, et al. Fatigue behaviour of FDM-3D printed polymers, polymeric composites and architected cellular materials. Int J Fatigue 2021;143:106007. https://doi.org/10.1016/j.ijfatigue.2020.106007.

[30] Anderegg DA, Bryant HA, Ruffin DC, Skrip SM, Fallon JJ, Gilmer EL, et al. In-situ monitoring of polymer flow temperature and pressure in extrusion based additive manufacturing. Addit Manuf 2019;26:76–83. https://doi.org/10.1016/j.addma.2019.01.002.

[31] Ahn SH, Montero M, Odell D, Roundy S, Wright PK. Anisotropic material properties of fused deposition modeling ABS. Rapid Prototyp J 2002;8:248–57. https://doi.org/10.1108/13552540210441166.

[32] Gao X, Qi S, Kuang X, Su Y, Li J, Wang D. Fused filament fabrication of polymer materials: A review of interlayer bond. Addit Manuf 2021;37:101658. https://doi.org/10.1016/j.addma.2020.101658.

[33] Kiendl J, Gao C. Controlling toughness and strength of FDM 3D-printed PLA components through the raster layup. Compos B Eng 2020;180:107562. https://doi.org/10.1016/j.compositesb.2019.107562.

[34] Webbe Kerekes T, Lim H, Joe WY, Yun GJ. Characterization of process–deformation/damage property relationship of fused deposition modeling (FDM) 3D-printed specimens. Addit Manuf 2019;25:532–44. https://doi.org/10.1016/j.addma.2018.11.008.

[35] Rezayat H, Zhou W, Siriruk A, Penumadu D, Babu S. Structure-mechanical property relationship in fused deposition modelling. Mater Sci Technol (United Kingdom) 2015;31:895–903. https://doi.org/10.1179/1743284715Y.0000000010.

[36] Wang L, Gardner DJ. Contribution of printing parameters to the interfacial strength of polylactic acid (PLA) in material extrusion additive manufacturing. Progr Additive Manuf 2018;3:165–71. https://doi.org/10.1007/S40964-018-0041-7.

[37] Rayegani F, Onwubolu GC. Fused deposition modelling (FDM) process parameter prediction and optimization using group method for data handling (GMDH) and differential evolution (DE). Int J Adv Manuf Technol 2014; 73(1): 509–519. https://doi.org/10.1007/S00170-014-5835-2.

[38] Ayatollahi MR, Nabavi-Kivi A, Bahrami B, Yazid Yahya M, Khosravani MR. The influence of in-plane raster angle on tensile and fracture strengths of 3D-printed PLA specimens. Eng Fract Mech 2020;237:107225. https://doi.org/10.1016/j.engfracmech.2020.107225.

[39] Marşavina L, Vălean C, Mărghitaş M, Linul E, Razavi SMJ, Berto F, et al. Effect of the manufacturing parameters on the tensile and fracture properties of FDM 3D-printed PLA specimens. Eng Fract Mech 2022;274. https://doi.org/10.1016/j.engfracmech.2022.108766.

[40] Liu Y, Bai W, Cheng X, Tian J, Wei D, Sun Y, et al. Effects of printing layer thickness on mechanical properties of 3D-printed custom trays. J Prosthet Dent 2020: 1–7. https://doi.org/10.1016/j.prosdent.2020.08.025.

[41] Mantecón R, Rufo-Martín C, Castellanos R, Díaz-Alvarez J. Experimental assessment of thermal gradients and layout effects on the mechanical performance of components manufactured by fused deposition modeling. Rapid Prototyp J 2022. https://doi.org/10.1108/RPJ-12-2021-0329.

[42] Seibert P, Susmel L, Berto F, Kästner M, Razavi SMJ. Applicability of strain energy density criterion for fracture prediction of notched PLA specimens produced via fused deposition modeling. Eng Fract Mech 2021;258. https://doi.org/10.1016/j.engfracmech.2021.108103.

[43] Marsavina L, Sapora A, Susmel L, Taylor D. The application of the Theory of Critical Distances to nonhomogeneous materials. Fatigue Fract Eng Mater Struct 2023:1–16. https://doi.org/10.1111/ffe.13922.

[44] Sharafi S, Santare MH, Gerdes J, Advani SG. A review of factors that influence the fracture toughness of extrusion-based additively manufactured polymer and polymer composites. Addit Manuf 2021;38:101830. https://doi.org/10.1016/j.addma.2020.101830.

[45] Gordelier TJ, Thies PR, Turner L, Johanning L. Optimising the FDM additive manufacturing process to achieve maximum tensile strength: a state-of-the-art review. Rapid Prototyp J 2019;25:953–71. https://doi.org/10.1108/RPJ-07-2018-0183.

[46] Aliheidari N, Christ J, Tripuraneni R, Nadimpalli S, Ameli A. Interlayer adhesion and fracture resistance of polymers printed through melt extrusion additive manufacturing process. Mater Des 2018;156:351–61. https://doi.org/10.1016/j.matdes.2018.07.001.

[47] Spoerk M, Arbeiter F, Cajner H, Sapkota J, Holzer C. Parametric optimization of intra- and inter-layer strengths in parts produced by extrusion-based additive manufacturing of poly(lactic acid). J Appl Polym Sci 2017;134:1–15. https://doi.org/10.1002/app.45401.

[48] ISO 527-1:2019, Plastics. Determination of tensile properties. Part 1: General principles, International Organization for Standardization; 2020.

[49] ISO 527-2:2012, Plastics. Determination of tensile properties. Part 2: Test conditions for moulding and extrusion plastics., International Organization for Standardization; 2012.

[50] Özen A, Auhl D, Völlmecke C, Kiendl J, Abali BE. Optimization of Manufacturing Parameters and Tensile. Materials 2021. https://doi.org/10.3390/ma14102556.

[51] ISO 178:2019, Plastics. Determination of flexural properties, International Organization for Standardization; 2020.

[52] Solav D, Moerman KM, Jaeger AM, Genovese K, Herr HM. MultiDIC: An open-source toolbox for multi-view 3D digital image correlation. IEEE Access 2018;6: 30520–35. https://doi.org/10.1109/ACCESS.2018.2843725.

[53] Zweben C, Smith WS, Wardle MW. Test Methods for Fiber Tensile Strength, Composite Flexural Modulus, and Properties of Fabric-Reinforced Laminates. ASTM Spec Tech Publ 1979:228–62. https://doi.org/10.1520/stp36912s.

[54] Taylor D. The Theory of Critical Distances. Chapter 2: The Theory of Critical Distances. Basics: An Introduction to the Basic Methodology of the TCD, Elsevier Science; 2007.

[55] Vincent PI. The necking and cold-drawing of rigid plastics. Polymer (Guildf) 1960;1:7–19. https://doi.org/10.1016/0032-3861(60)90003-3.

[56] Considére M. Mémoire sur l'emploi du fer et de l'acier dans les constructions. Annales Des Ponts et Chaussées 1885:574–605.

[57] Van Krevelen DW, Te Nijenhuis K. Mechanical Properties of Solid Polymers 2009. https://doi.org/10.1016/b978-0-08-054819-7.00013-3.

[58] Ferreira RTL, Amatte IC, Dutra TA, Bürger D. Experimental characterization and micrography of 3D printed PLA and PLA reinforced with short carbon fibers. Compos B Eng 2017;124:88–100. https://doi.org/10.1016/j.compositesb.2017.05.013.

[59] Khosravani MR, Berto F, Ayatollahi MR, Reinicke T. Characterization of 3D-printed PLA parts with different raster orientations and printing speeds. Sci Rep 2022;12:1–10. https://doi.org/10.1038/s41598-022-05005-4.

[60] Taylor D. Applications of the Theory of Critical Distances to the prediction of Brittle Fracture in Metals and Non-Metals. In: 15th European Conference of Fracture (ECF15); 2004, p. 1–8.

[61] Fernandez-Vicente M, Calle W, Ferrandiz S, Conejero A. Effect of Infill Parameters on Tensile Mechanical Behavior in Desktop 3D Printing, 3D Print. Addit Manuf 2016;3:183–92. https://doi.org/10.1089/3dp.2015.0036.

[62] Cole DP, Riddick JC, Iftekhar Jaim HM, Strawhecker KE, Zander NE. Interfacial mechanical behavior of 3D printed ABS. J Appl Polym Sci 2016;133. https://doi.org/10.1002/app.43671.

[63] Özen A, Abali BE, Völlmecke C, Gerstel J, Auhl D. Exploring the Role of Manufacturing Parameters on Microstructure and Mechanical Properties in Fused Deposition Modeling (FDM) Using PETG. Appl Compos Mater 2021;28:1799–828. https://doi.org/10.1007/s10443-021-09940-9.

[64] Somireddy M, Czekanski A, Singh CV. Development of constitutive material model of 3D printed structure via FDM. Mater Today Commun 2018;15:143–52. https://doi.org/10.1016/j.mtcomm.2018.03.004.

[65] Akhoundi B, Behravesh AH. Effect of Filling Pattern on the Tensile and Flexural Mechanical Properties of FDM 3D Printed Products. Exp Mech 2019;59:883–97. https://doi.org/10.1007/s11340-018-00467-y.

[66] Taylor D. Polymers: Brittle Fracture in Polymeric Materials. The Theory of Critical Distances 2007:93–118. https://doi.org/10.1016/B978-008044478-9/50007-7.

[67] Ward IM, Sweeney J. Yielding and Instability in Polymers. Mech Properties Solid Polym 2012:319–78. https://doi.org/10.1002/9781119967125.CH12.

[68] Ward IM, Sweeney J. Breaking Phenomena. Mechanical Properties of Solid Polymers 2012; 319–378. https://doi.org/10.1002/9781119967125.CH13.